Rae, A. S.P. et al. (2019) Impact-induced porosity and microfracturing at the Chicxulub impact structure. *Journal of Geophysical Research: Planets*, (doi:10.1029/2019JE005929).

There may be differences between this version and the published version. You are advised to consult the publisher's version if you wish to cite from it.

This is the peer reviewed version of the following article: Rae, A. S.P. et al. (2019) Impact-induced porosity and microfracturing at the Chicxulub impact structure. *Journal of Geophysical Research: Planets*, which will be published in final form at 10.1029/2019JE005929. This article may be used for non-commercial purposes in accordance with Wiley Terms and Conditions for Self-Archiving.

http://eprints.gla.ac.uk/192904/

Deposited on: 13 August 2019

Enlighten – Research publications by members of the University of Glasgow
http://eprints.gla.ac.uk

Impact-induced Porosity and Micro-fracturing at the Chicxulub Impact Structure

Auriol S. P. Rae[1,2], Gareth S. Collins[1], Joanna V. Morgan[1], Tobias Salge[3], Gail L. Christeson[4], Jody Leung[1], Johanna Lofi[5], Sean P. S. Gulick[4], Michael Poelchau[2], Ulrich Riller[6], Catalina Gebhardt[7], Richard A. F. Grieve[8], Gordon R. Osinski[8], IODP-ICDP Expedition 364 Scientists

[1]Department of Earth Science and Engineering, Imperial College London, London, UK, SW7 2BP
[2]Institut für Geo- und Umweltnaturwissenschaften, Albert-Ludwigs-Universität Freiburg, Geologie, 79104 Freiburg, Germany
[3]Imaging and Analysis Centre, Natural History Museum, London, UK, SW7 5BD
[4]Institute for Geophysics and Department of Geological Sciences, Jackson School of Geosciences, University of Texas at Austin, Austin, TX, USA
[5]Gèosciences Montpellier, Universitè de Montpellier, Montpellier, France
[6]Institut für Geologie, Universität Hamburg, Bundesstrasse 55, 20146 Hamburg, Germany
[7]Alfred Wegener Institute Helmholtz Centre of Polar and Marine Research, Bremerhaven, Germany.
[8]Department of Earth Sciences / Centre for Planetary Science and Exploration, Western University, London, Ontario, N6A 3K7, Canada

Key Points:

- The Chicxulub peak ring is extremely porous and low density due to pervasive shock-induced micro-fracturing.
- The present-day orientation of micro-fractures is a consequence of the orientation of stress during shock and subsequent rotation during crater formation.
- Shear-induced dilatancy is an important cause of gravity anomalies in large complex craters.

Corresponding author: Auriol S. P. Rae, auriol.rae@geologie.uni-freiburg.de

Abstract

Porosity and its distribution in impact craters has an important effect on the petrophysical properties of impactites: seismic wave-speeds and reflectivity, rock permeability, strength, and density. These properties are important for the identification of potential craters and the understanding of the process and consequences of cratering. The Chicxulub impact structure, recently drilled by the joint International Ocean Discovery Program and International Continental scientific Drilling Program Expedition 364, provides a unique opportunity to compare direct observations of impactites with geophysical observations and models. Here, we combine small scale petrographic and petrophysical measurements with larger scale geophysical measurements and numerical simulations of the Chicxulub impact structure. Our aim is to assess the cause of unusually high porosities within the Chicxulub peak ring and the capability of numerical impact simulations to predict the gravity signature and the distribution and texture of porosity within craters. We show that high porosities within the Chicxulub peak ring are primarily caused by shock-induced micro-fracturing. These fractures have preferred orientations, which can be predicted by considering the orientations of principal stresses during shock, and subsequent deformation during peak-ring formation. Our results demonstrate that numerical impact simulations, implementing the Dynamic Collapse Model of peak-ring formation, can accurately predict the distribution and orientation of impact-induced micro-fractures in large craters which plays an important role in the geophysical signature of impact structures.

Plain Language Summary

The Chicxulub crater, Mexico, is widely known for its association with the extinction of the non-avian dinosaurs at the end of the Cretaceous period. The crater was first identified due to its gravitational and magnetic anomalies. Potential impact structures are often identified, in part, on the basis of geophysical anomalies; most commonly including a circular gravity low. Gravity is slightly weaker at craters because the impact cratering process removes mass from the impact site. In this study, we examine the cause of the Chicxulub gravity anomaly by combining observations from recent drilling of the crater, geophysical data measured across the crater, and numerical impact simulations. We demonstrate that porosity in rocks beneath the crater floor is primarily accommodated by fracturing during the impact cratering process, that the orientation of those fractures are consistent with predictions from numerical impact simulations, and that impact-induced porosity is one of the primary causes of gravity anomalies in large impact craters.

1 Introduction

Impact cratering is the dominant surface process on most rocky bodies of the Solar System. The process of hypervelocity impact causes irreversible changes to the nature and physical properties of rocks (Melosh, 1989). These changes produce anomalies in geophysical data that make craters conspicuous in comparison to the surrounding rocks. The identification of potential craters, on Earth and, increasingly, across the Solar System, e.g., Zuber et al. (2013), is primarily achieved by remote geophysical surveying.

The most commonly observed geophysical signature of an impact structure is a circular region of negative residual gravity (Pilkington & Grieve, 1992). Negative residual gravity anomalies at craters are caused by the replacement of high density intact rocks in the pre-impact target with fractured para-autochthonous rocks, porous impact breccias, and/or the relative loss of mass due to excavation and basin infill (whether it is filled by atmosphere, water, post-impact sedimentary rocks, or vacuum). Within complex craters, which are shallow compared to their diameters, the main contributor to the gravity signature derives from fractured para-autochthonous target rocks beneath the floor of the crater (Pilkington & Grieve, 1992). Additionally, large complex craters (> 40 km) may

have relative gravity highs in their center due to the uplift of high-density material from depth during cratering. The presence of low-density, porous rocks in impact structures has important implications for the transport of fluids within craters: affecting the viability and longevity of hydrothermal activity, e.g., Abramov and Kring (2007), the distribution of potential hydrocarbon reservoirs (Grieve, 2005), and the habitability of impact structures for microbial life (Cockell, 2006). Consequently, understanding how small-scale properties of impactites link to the large-scale geophysical characteristics of craters is of critical importance.

Impact simulations are now capable of modeling the tendency of rocks and granular materials to change volume during shear failure, i.e., dilatancy. Results of impact simulations using this model are consistent with porosity measurements and the gravity anomalies of simple craters (Collins, 2014) . However, limited porosity data have hindered comparisons with complex craters. Furthermore, whilst the importance of fracturing in reducing the density of para-autochthonous impactites has been widely acknowledged, detailed analysis of the micro-porosity and micro-fracturing of shocked para-autochthonous rocks (e.g., Winkler et al. (2018)) is limited, particularly for naturally shocked rocks.

Here, the Chicxulub impact structure is used as a case-study to understand the production of porosity during complex crater formation. We analyze the petrophysical and micro-structural character of uplifted basement rocks in the Chicxulub peak ring and, through numerical impact simulations, link our results to the gravity signature across the crater. Our study provides insight into the formation of complex craters and, more specifically, the processes that produce the remarkable physical properties of impact-deformed rocks.

1.1 The Chicxulub Impact Structure and IODP-ICDP Expedition 364

The Chicxulub structure, located in the Yucatán peninsula of Mexico, is a 190–210 km diameter impact structure (Figure S1b). Its identification was first made on the basis of large-scale geophysical signatures: a large, circular, negative Bouguer gravity anomaly and magnetic anomalies (Penfield & Camargo, 1981; Hildebrand et al., 1991). The only surface expression of the crater's presence is a semi-circular ring of water-filled sinkholes, cenotes, in the Cenozoic limestones that overlie the onshore portion of the crater.

Following the discovery of the crater, several attempts were made to constrain the size and structure of the Chicxulub crater based on forward modeling of potential field data (Hildebrand et al., 1991; Sharpton et al., 1993; Hildebrand et al., 1995; Sharpton et al., 1996; Espindola et al., 1995). The variations between the models, in terms of structure and the density contrasts between lithologies, attest to the nonuniqueness of gravity modeling.

Seismic reflection and refraction surveys were carried out at Chicxulub to resolve the crater dimensions and sub-crater structure (Morgan et al., 1997; Gulick et al., 2008). The results of those surveys indicated that the topographic (inner) rim of the crater is 140–170 km in diameter (beyond which are outer ring faults), with a floor approximately 1 km beneath the surface, and an 80–90 km diameter peak ring which rises up to 400 m above the crater floor (Gulick et al., 2013). Beneath the crater center, the mantle has been uplifted by 1.5–2 km (Christeson et al., 2009). The basement, both outside and deep beneath the crater, possesses seismic velocities > 5.8 km s^{-1}(Christeson et al., 2001), indicating that the pre-impact crust, beneath the sedimentary cover, consisted of high density, non-porous rocks. A ring-shaped Bouguer gravity minimum within the crater corresponds to a radial distance slightly interior to the peak ring. Additionally, beneath the peak ring a strong inward-dipping reflector can be observed. Together, these observations indicate that the rocks of the peak ring, and its roots which dip inwardly, are among the lowest density para-autochtonous rocks within the crater. A detailed review of the geophysical characteristics of the Chicxulub structure can be found in Gulick et al. (2013).

In 2016, a joint expedition of the International Ocean Discovery Program and International Continental scientific Drilling Program (IODP-ICDP Expedition 364) drilled into the peak ring of the Chicxulub structure (Figure S1c). The expedition recovered core between 505.42 and 1334.69 mbsf (meters below sea floor) including, from 750.25–1334.69 mbsf, a sequence of uplifted granitic target rocks, with occasional sheet intrusions of pre-impact igneous rocks and impact-related breccias and melt rocks. A schematic lithological column and location map is shown in Figures S1a and S1b respectively.

Physical property data from the expedition (Morgan et al., 2017; Christeson et al., 2018) have shown that the shocked target rocks within the Chicxulub peak ring have porosities of approximately 10%, which is a likely cause of the gravity minimum associated with the peak ring. However, the micro-structural cause of this porosity is uncertain and it is not known how porosity is more widely distributed across the crater.

Here, we assess the cause of the unusually low densities and high porosities of the uplifted granitic rocks of the Chicxulub peak ring. These results help constrain cratering-related deformation mechanisms and the timing of porosity-generation. Observational results are obtained by petrophysical and petrographic techniques, with additional data from remote geophysical surveys. The observational data are then compared to the results of numerical impact simulations which can predict porosity distribution and micro-fracture orientations.

2 Data Sets

2.1 Geophysical and Petrophysical data

2.1.1 Gravity Data

Numerous gravity surveys have been acquired at the site of the Chicxulub structure. Data used here (Figure S1b) were provided by Alan Hildebrand and Mark Pilkington (see Pilkington et al. (1994)), supplemented by data acquired during the 2005 seismic surveying of the structure (see Gulick et al. (2008)). Comparison between the results of numerical impact simulations and gravity data requires the determination of an average gravity profile across the structure, without any regional gravity effects. Following Vermeesch et al. (2009), data were initially transformed to a cartesian coordinate system with an origin at the crater center (21.31°N, 270.46°E):

$$X = (101.71 \times Longitude) + 9107.56 \ , \tag{1}$$

$$Y = (112.02 \times Latitude) - 2386.67 \ . \tag{2}$$

The gravity data were then corrected to account for the regional variation of the Bouguer gravity field across the site. This correction was achieved by excluding all data within 100 km of the crater center, and fitting a best-fit plane through the remaining regional data set. The best-fit plane, representing the regional Bouguer gravity field, Z, takes the form:

$$Z = 227.2 + 0.04641X + 0.7371Y \ . \tag{3}$$

After correction of the Bouguer gravity data to account for the regional field, radial profiles were acquired in 1° intervals. These radial profiles avoided anomalous regions of the gravity field to the south and north-west of the crater center (Figure 1a). From the 232 remaining radial profiles, the median and quartile values of the radial residual gravity field were determined with increasing radial distance (Figure 1b). The effect

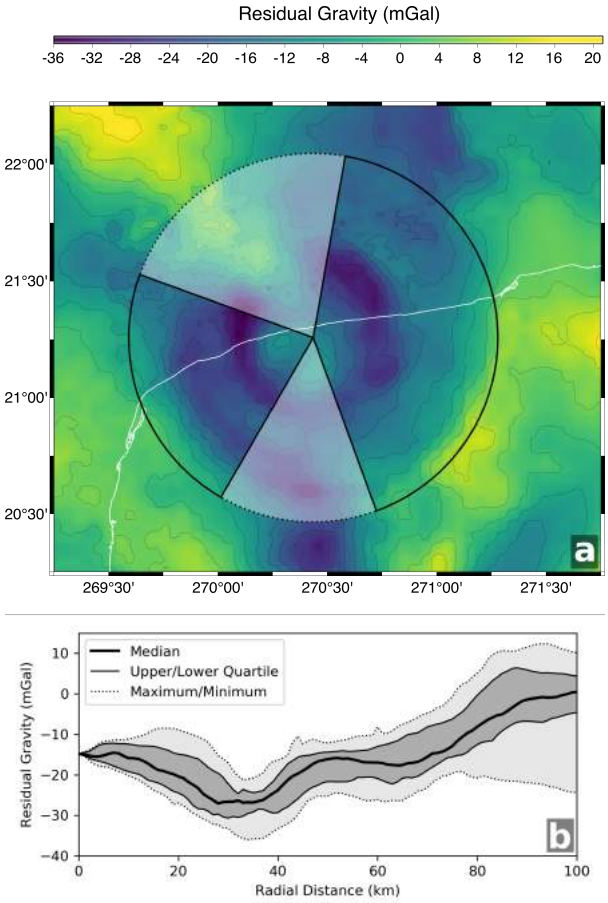

Figure 1. a) Residual Bouguer gravity map of the crater, with data contoured at 5 mGal intervals. The circle marks the area within 100 km of the crater center, shaded sectors indicate the regions from which no gravity profiles were obtained during the calculation of b) the average (median) radial gravity profile of the Chicxulub structure. Upper and lower quartiles, and minimum and maximum values are indicated.

of removing profiles from the anomalous regions can be seen in the **Supplementary Material** (Figure S2).

2.1.2 Expedition Data

IODP-ICDP Expedition 364 collected density data from cores using two different methods. First, cores were analyzed with a Geotek Multi-Sensor Core Logger (MSCL) which, alongside other physical property measurements, measured bulk density by gamma ray attenuation (GRA). These measurements were acquired at 2 cm intervals where, due to the machine set-up, the individual resolution was 0.5 cm (see Morgan et al. (2017) for details). The second set of density data derives from He-pycnometry measurements (Quantachrome pentapycnometer) of discrete samples taken from the core. Samples had a diameter of 2 cm and an approximate volume of 6 cm^3. Samples were taken approximately once per core section ($\sim$ every 1.2 m), and a total of 719 samples were measured. He-pycnometry, in addition to allowing determination of bulk density, also allows the determination of grain density and porosity (see Morgan et al. (2017) for details).

The raw expedition data are shown within the **Supplementary Material** (Figure S3). Here, we have processed the data acquired during Expedition 364 in order to facilitate direct comparison between the results of numerical simulations and the observations, and between the two observational methods. Firstly, all data from lithologies that were not granitic target rocks were excluded; numerical simulations are not capable of modeling the injection of allochthonous impactites into the target rocks, nor can they model fine-scale lithological variations between subvolcanic intrusive rocks and basement rocks. Subsequent data processing involved the calculation of a running average and standard deviation within ±6 m of each He-pycnometry sample. Averages and standard deviations were only calculated where three or more measurements were acquired within the 12 m wide interval. Comparable measurements from the MSCL data were acquired by taking an average and standard deviation corresponding to the same depth interval for each He-pycnometry sample.

2.2 SEM Imaging and Analysis

To understand the micro-structural cause of the porosity within the granitic basement rocks, 10 thin sections were prepared from samples of the recovered granitic target rocks at different depths within Hole M0077A. Backscattered electron (BSE) images of the thin sections were obtained using a Zeiss Ultra Plus field emission scanning electron microscope (SEM) with the large-area imaging software and hardware package, ZEISS Atlas 5, at the Natural History Museum, London. Individual images were obtained with an accelerating voltage of 20 kV using the backscattered electron (BSE) detector, a working distance of 8.0 mm, and a resolution of 748.9 nm/pixel. The Atlas 5 software was then used to stitch the individual images from a section to produce a single composite image. The total areas of each stitched image are shown in Table S1. As a consequence of the pixel size, and due to Nyquist's Theorem, the minimum width of a pore that can be accurately resolved in these images is ~ 1.5 μm.

Image processing was carried out in order to analyze and quantify porosity within the thin sections. Processing was achieved using the ImageJ software package (Schindelin et al., 2012). The first stage required to analyze porosity is image thresholding. The images were deliberately acquired such that there was a significant contrast of greyscale values between pores (black), and mineral phases (grey to white). ImageJ provides several algorithms that automatically thresholds images into objects (pores) and background (solid material), resulting in an image consisting of only binary values, black for pores and white for background. Here, the default ImageJ thresholding algorithm was used, and the result then manually checked and, if required, adjusted.

Once pores were thresholded into a binary image file, porosity estimates could be made by assuming the application of the Delesse principle; that the volume fraction of pores can be estimated by calculating the area fraction of pores in a 2D image. Additionally, the orientation and aspect ratio of each pore were determined by fitting ellipses to each pore, an available function in ImageJ.

2.3 The iSALE Shock Physics Code

We simulated the formation of the Chicxulub impact structure using the iSALE shock physics code. iSALE is a multi-rheology, multi-material code based on the SALE hydrocode (Amsden et al., 1980). The original code has been modified to include: an elasto-plastic constitutive model, fragmentation models (Melosh et al., 1992), various equations of state (Ivanov et al., 1997), a porous compaction model (Wünnemann et al., 2006), and a dilatancy model (Collins, 2014). iSALE and its precursor codes, SALES-2 (Collins et al., 2002) and SALE-B (Ivanov, 2005) have been used to simulate the formation of the Chicxulub impact structure in previous studies (Collins et al., 2002; Ivanov, 2005; Collins et al., 2008; Morgan et al., 2016; Rae et al., 2019). Here, we use the model pa-

rameters presented by Rae et al. (2019), where a 12 km diameter spherical impactor, using an equation of state for granite with a density of 2630 kg m^{-3} strikes a three layer target at 15 km s^{-1}. The three layer target is composed of: a 3 km layer of sedimentary rocks, represented with an equation of state for calcite, overlying a 30 km layer of crystaline basement rocks, represented with an equation of state for granite, overlying mantle, represented with an equation of state for dunite. This simulation was run at a resolution of 60 cells per projectile radius, i.e. cell widths of 100 m. A complete list of the parameters used in our simulation is shown in the **Supplementary Material** (Tables S2 and S3).

Predicting the gravity signal of an impact structure in a numerical model requires a dilatancy model. Dilatancy is the tendency of granular and rocky materials to undergo volume change when subjected to shear deformation Collins (2014) describes the dilatancy model used in iSALE. The equation used to update the distension in iSALE computational cells undergoing shear deformation is:

$$\frac{d\alpha}{dt} = \alpha\beta\frac{d\gamma_p}{dt} \ , \tag{4}$$

where the first term, α, is the distension, which can be defined as a function of porosity, $\frac{1}{1-\phi}$. The final term of Equation 4 is the plastic shear strain rate, which is determined based on velocity gradients in the cell. The second, and most important term in Equation 4 is known as the dilatancy coefficient, β, which describes the material's tendency to gain volume upon plastic shear strain, and is a function of pressure (p), temperature (T), and the pre-existing distension (α) of the material (see Table S3):

$$\beta = \beta_{max}(\frac{\alpha_c - \alpha}{\alpha_c - \alpha_{min}})(1 - \frac{log(p/10^5)}{log(p_{lim}/10^5)})tanh[\xi(\frac{T}{T_m} - 1)] \ . \tag{5}$$

β_{max} is a material specific value, where large values indicate a large tendency to dilate upon shear deformation. For impact cratering simulations, and large-scale numerical simulations of rock masses, Collins (2014) suggests that β_{max} values range between 0.045–0.180, where $\beta_{max} = 0.045$, corresponding to a Low Geological Strength Index (GSI) material, provides the best fit to the gravity and porosity data of simple craters and small complex craters. Here, that value is used to test its applicability to larger complex craters.

From a simulation with this dilatancy model, it is possible to calculate the resultant gravity anomaly associated with the simulated crater including: the effects of density reduction due to shear-induced dilatancy and the filling of the impact crater with post-impact sedimentary rocks. Gravity profiles are calculated by using the modelled distension field generated by iSALE; distension values are converted to a mass difference by assigning a reference density to each of the materials in the simulation, this assigned reference density can be varied independently from the reference density in the equation of state of the material. The additional effect of low-density crater fill can then be included by filling, to whatever depth required, the modelled crater with a material of an assigned density. Finally, the effect of erosion can be considered by removing any material above a specified depth. High density impact melt rocks are accounted for in this calculation because materials approaching or above their melting temperature have suppressed dilatancy. However, due to the simplifications of the model, pre-impact vertical variations in crustal composition, and therefore density, are not accounted for. Crustal density is generally be expected to increase with depth, therefore the gravity calculation is likely to underestimate the mass excess of the central uplift and overestimate the excess outside of the central uplift.

3 Results

3.1 Geophysical and Petrophysical Data

The processed residual 2D gravity profile (Figure 1b) possesses a local gravity high in the crater center of -15 mGal. At 30–40 km radial distance, a gravity low of approximately -25 mGal can be observed, beyond which the gravity signal increases to match the regional gravity field. Beyond 80 km, the interquartile range of the radial gravity signal increases due to thickness variations of the Mesozoic and Cenozoic sedimentary rocks at various azimuths. The region to the north-east of the crater contains a thicker sequence of sedimentary rocks, and therefore has a more negative residual gravity signal. The features of the average gravity profile are broadly consistent with the features seen in previously published individual profiles and average profiles (e.g., Sharpton et al. (1993)). Additionally, the total mass deficit associated with the Chicxulub impact structure can be calculated from the gravity anomaly by applying Gauss's theorem (see Campos-Enriquez et al. (1998)). The average gravity profile obtained here suggests a total mass deficit of 9.15×10^{15} kg. Upper and lower bounds on the deficit can be made using the upper and lower quartile profiles, which suggest mass deficits between 4.90×10^{15} kg and 1.25×10^{16} kg respectively. These values are consistent with previous estimates of the Chicxulub mass deficit (Campos-Enriquez et al., 1998).

The low seismic velocities of the Chicxulub peak ring, combined with the large gravity low slightly within the peak ring, had suggested, prior to drilling, that the Chicxulub peak ring is composed of unusually low density rocks (Morgan et al., 2000). Results from Expedition 364 have shown that the peak ring is composed of uplifted crystalline target rocks that possess unusually low densities and high porosities compared to typical crystalline basement rocks (Christeson et al., 2018). Processed expedition data are shown in Figure 2. The target rocks possess consistent and typical grain densities for granite, averaging 2628 ± 39 kg m^{-3} (1σ), but have remarkably high porosities. The average porosity of the granitic target rocks is $11.5 \pm 4.7\%$, resulting in average bulk densities of 2444 ± 75 kg m^{-3}; additionally, the raw porosity measurements show that the granitic target rocks have a pervasive baseline porosity of approximately 8%, where few samples possess less porosity, but where local excursions to higher porosities occur. There is some heterogeneity of porosity and bulk density with depth in the recovered core: in the upper 100 m, average porosities increase beyond 20% and the variability increases up to $\sigma = 8.1\%$. Additionally, porosities within granitic rocks beneath 1225 mbsf increase from <10% to >10%. Despite some discrepancy between bulk density measurements by He-pycnometry and the independently measured bulk density by GRA using the MSCL, particularly from depths below 1075 mbsf, the 1σ envelopes of both measurements always overlap, indicating full consistency between the data sets.

3.2 SEM imaging and Analysis

Inspection of the SEM images shows that the largest contributor to the total porosity of the granitic target rocks is by intra-granular fracturing, with additional contribution from cataclasites and large inter-granular pores (Figure 3). Cataclasites are easily distinguished by their finer-grain sizes, increased grain angularity, and increased porosity relative to their host material, whilst large inter-granular pores are defined by their anomalous sizes compared to the other sources of porosity (see **Supplementary Material**, Figures S4-13). Across all the thin sections, the average fraction of the porosity contributed by intra-granular fractures is 0.55, while the average fraction of porosity contributed by inter-granular pores and cataclasites are 0.24 and 0.21, respectively.

Excluding the large inter-granular pores and cataclasites, the average porosity of the intra-granularly fractured granites is 6.4%. This intra-granular fracturing is distributed heterogeneously throughout the thin sections, and is primarily dependent upon the mineral that is fractured (Figure 4). The three major rock-forming minerals within the gran-

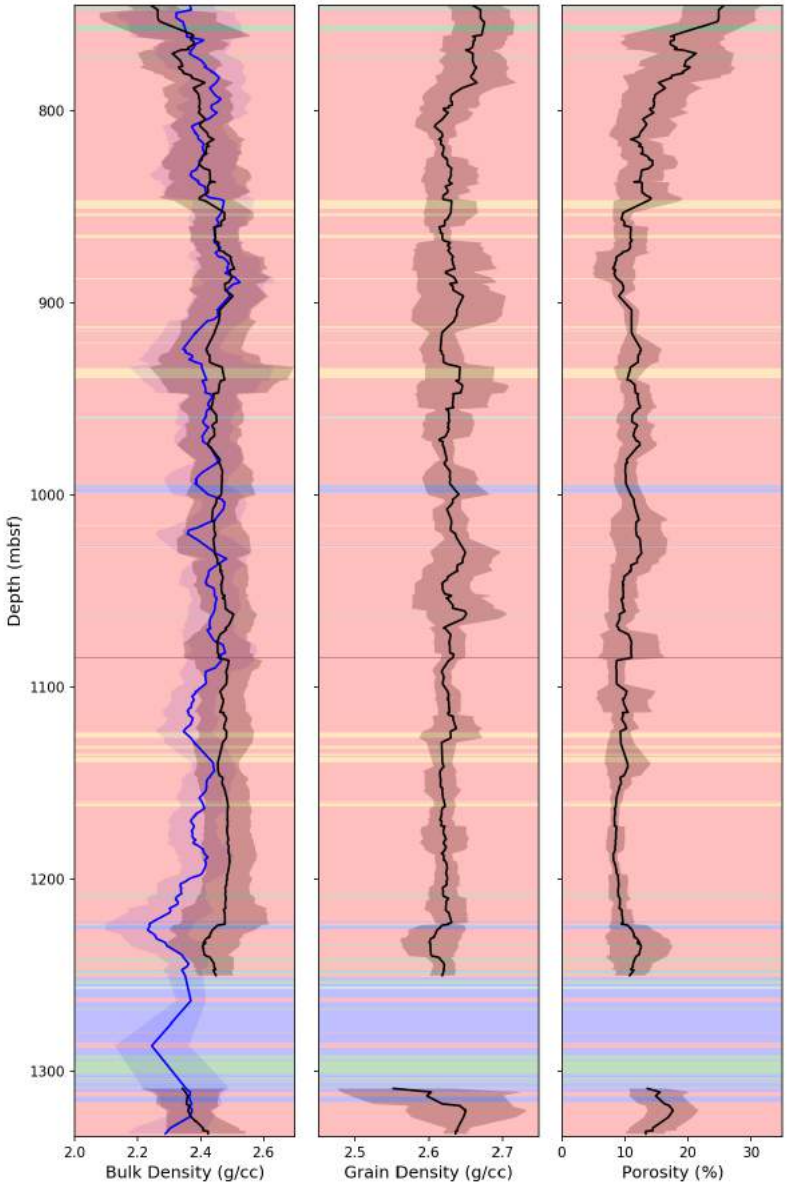

Figure 2. Processed physical property measurements of the granitic rocks recovered during Expedition 364. Black lines indicate moving averages of discrete sample measurements within a 12 m window, while 1σ distribution envelopes are indicated by the grey areas. The blue line and area on the bulk density profile (left) indicates the moving average and distribution envelope associated with MSCL measurements of bulk density using GRA. Background colours indicate the stratigraphy of Hole M0077A (see Figure S1): pink — Granitic Basement, blue — Suevitic Breccia, green — Impact Melt Rocks, orange — Pre-impact Igneous Dikes, and grey — Pg Sedimentary Rocks.

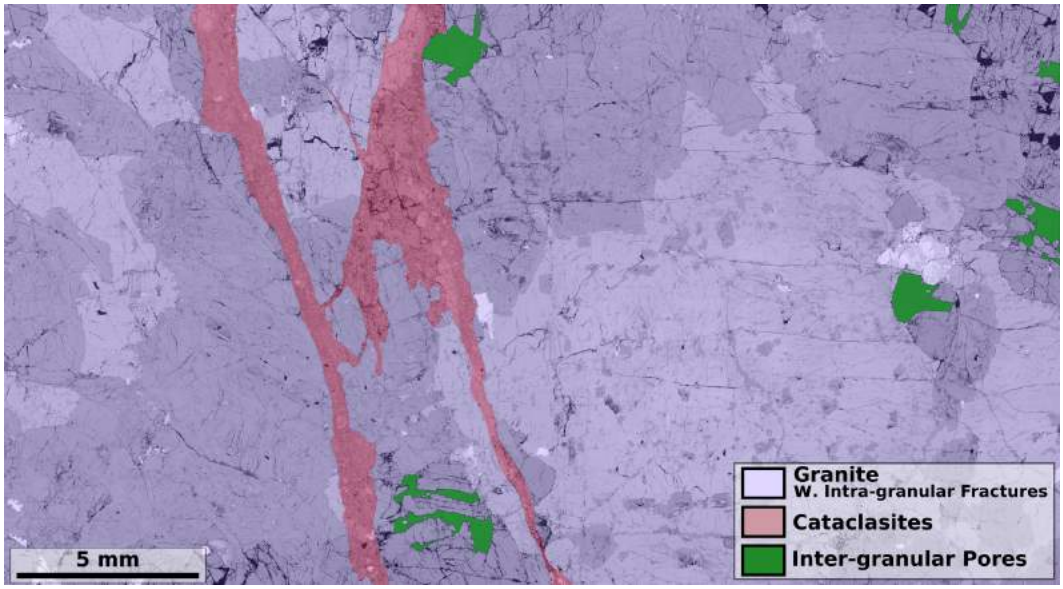

Figure 3. Whole thin-section BSE SEM image of Sample 364-77-A-276-R-1-17-19 (1249.52 mbsf) with color overlay to distinguish between the three types of porosity. The largest region, highlighted in pale blue, is dominated by intra-granular fractures. The region highlighted in red indicates a cataclasite network. Finally, the pores highlighted in green are the large inter-granular pores, almost certainly produced during sectioning.

ites are alkali feldspar, quartz, and plagioclase feldspar. Quartz grains are pervaded by planar fracture (PF) sets which rarely span the entire grain and which occasionally have feather feature (FF) lamellae (Figure 4a,e; Poelchau and Kenkmann (2011)). Additionally, the quartz grains possess occasional individual shear fractures on planar surfaces with observable sub-mm displacements, and rare non-planar fractures which typically contain a gouge of angular to sub-angular quartz fragments. Compared to the feldspars, the quartz grains are more porous. Plagioclase feldspar, whilst also pervasively micro-fractured, possesses a distinctly different fracture pattern to the quartz grains. The micro-fractures are typically closer-spaced than in quartz from the same sample, are rarely planar, and typically branch and converge into other fractures (Figure 4b,d). While the plagioclase crystals often have higher fracture densities than the quartz grains, the total dilation on each intra-granular plagioclase fracture is significantly smaller than the intra-granular fractures in quartz. Compared to the quartz and plagioclase feldspar within the granitic rocks from Hole M0077A, alkali feldspar is remarkably unfractured (Figure 4c), possessing only widely-spaced non-planar fractures.

Additional porosity in the granitic rocks is produced by cataclasites. These regions of the thin sections have extremely high porosities. Across the 4 thin sections that contain cataclasites, the average porosity in the cataclasite regions is 15.8%. Nevertheless, the cataclasites are only a small area of the total rock mass (20.0% of the total imaged area) and thus contribute only a small fraction of the total porosity of the thin sections. The SEM images show examples of cross-cutting relationships between the cataclasites and grains with intra-granular fractures (Figure 4f) that show the cataclasites formed after pervasive fracturing of the target rocks, also described by Riller et al. (2018) . Additionally, Riller et al. (2018) have shown that the cataclasites are truncated by later deformation events associated with crater formation.

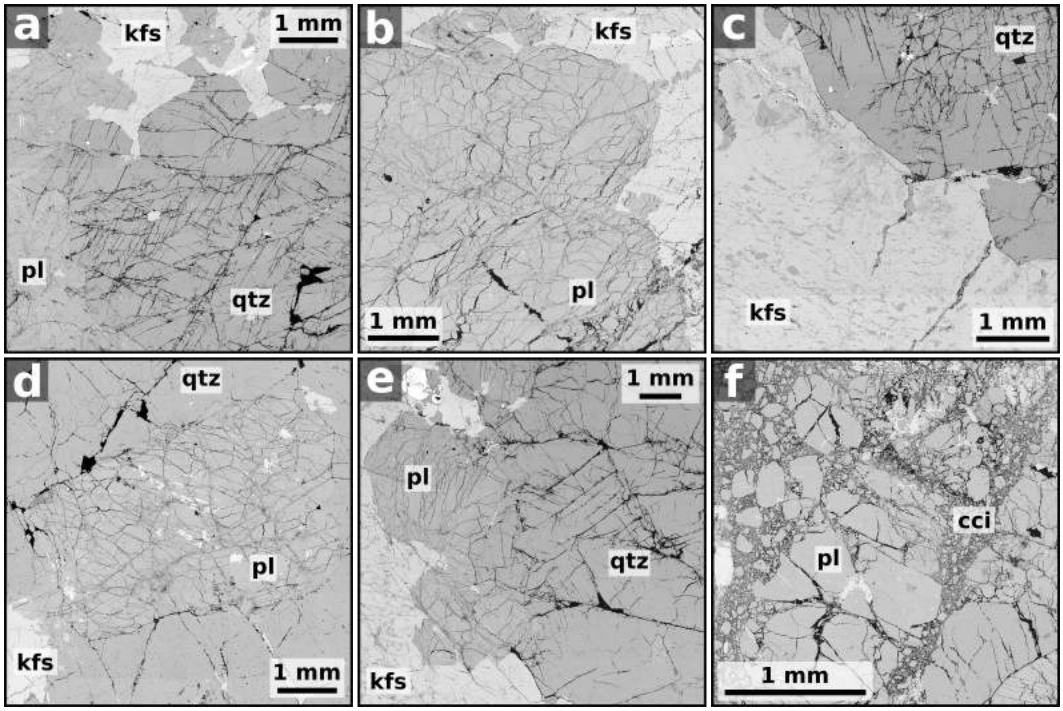

Figure 4. Intra-granular fractures within granitic minerals of the Chicxulub Peak Ring, qtz = Quartz, kfs = Alkali Feldspar, pl = Plagioclase, and cci = Cataclasite. a) Strongly dilated micro-fracture network in quartz. b) Poorly dilated, diverging and converging micro-fracture network in plagioclase. c) Poorly fractured alkali feldspar crystal contrasted with heavily fractured quartz. d) High density, poorly dilated, diverging and converging fracture network in a plagioclase grain surrounded by quartz with low density fractures. e) Fractured quartz, plagioclase, and alkali-feldspar with distinctly different micro-fracture patterns. f) Cataclasite partially incorporating a pre-fractured plagioclase grain.

The large inter-granular pores observed in the samples are almost certainly not representative of the in-situ porosity of the granitic target rocks. Their extreme sizes within the pore-size distributions (see **Supplementary Material**, Figures S4-13) of each sample indicate that they are mostly non-natural pores, i.e. produced during sample preparation. Nevertheless, the possibility remains that thin sections are too small to encompass the full pore-size distribution of these rocks. Regardless of their origin, the total contribution of these large inter-granular pores to the total porosity is equal to the average contribution from cataclasites and significantly less than the contribution from intra-granular fractures. These pores can only be found in 4 of the 10 thin sections, all deriving from near to the top of the hole.

Total porosity measurements obtained from SEM image analysis, subdivided by the source of porosity, are shown on Figure 5. In general, the estimations from SEM image analysis are consistent with the measurements made by He-pycnometry. All results from SEM analysis, excluding the upper-most thin section, fall within the 1σ envelope of the He-pycnometry porosity measurements. However, most of the SEM-derived porosities are offset to lower values compared to the mean measurement from He-pycnometry, and this would be exaggerated by excluding the large inter-granular pores, many of which are due to sample preparation. Potential errors associated with calculating porosity from SEM images include: lack of resolution to quantify pores smaller than ~ 1.5 μm, large pores distributed on a scale larger than a thin section (2–3 cm), porosity anisotropy, and sample preparation artifacts.

Quartz develops a number of unique deformation features over a range of shock-wave pressures (French & Koeberl, 2010). One of these features is PFs, which can occur in one or multiple orientations. The large abundance of PF sets in quartz from Hole M0077A, together with the inter-connectedness of the intra-granular fractures, suggests that most of the intra-granular fracturing is related to deformation during shock (Figure 4a,c,e). The partial disaggregation of some grains of quartz and plagioclase feldspar along intra-granular fractures into cataclasites and the matrix of monomict granitic breccias, indicates that the formation of cataclasites and brecciation occurred after the formation of intra-granular fractures (Figure 4f).

The orientation of pores within the thin sections is generally anisotropic (Figure 6). Six thin sections have unimodal pore orientation-frequency distributions while two more thin sections have a bimodal distribution (Table 1). Comparing these distributions to the images they derive from (Figure S14) indicates that the cause of the high frequency orientations is the orientation of PFs in quartz.

3.3 Numerical Simulations

Our numerical simulations of the Chicxulub impact event follow a model of the formation of peak rings, sometimes called the Dynamic Collapse Model, that has been developed over a number of decades (Grieve et al., 1981; Collins et al., 2002; Kring et al., 2016; Morgan et al., 2016). Within this model, and our simulation, the formation of a peak ring results from the over-heightening of a central uplift, and its subsequent lateral emplacement over the collapsed transient cavity rim (Figure S15). The simulation presented here, from Rae et al. (2019), allows predictions of the distribution and timing of porosity to be made. Porosity generation in rocks during complex crater collapse would be expected throughout the crater due to shear failure. The final distribution of modeled porosity caused by this dilatancy is shown in Figure 7a.

From the final simulated distribution of porosity in the structure it is possible to produce a vertical profile of porosity in the peak ring that can be compared to observational results (Figure 7c). Using $\beta_{max} = 0.045$, these results predict that the porosity of the peak ring material should be approximately $7 \pm 2\%$. Uncertainty in the exact comparative location between the model and the drilled core results in the $\pm$ 2% er-

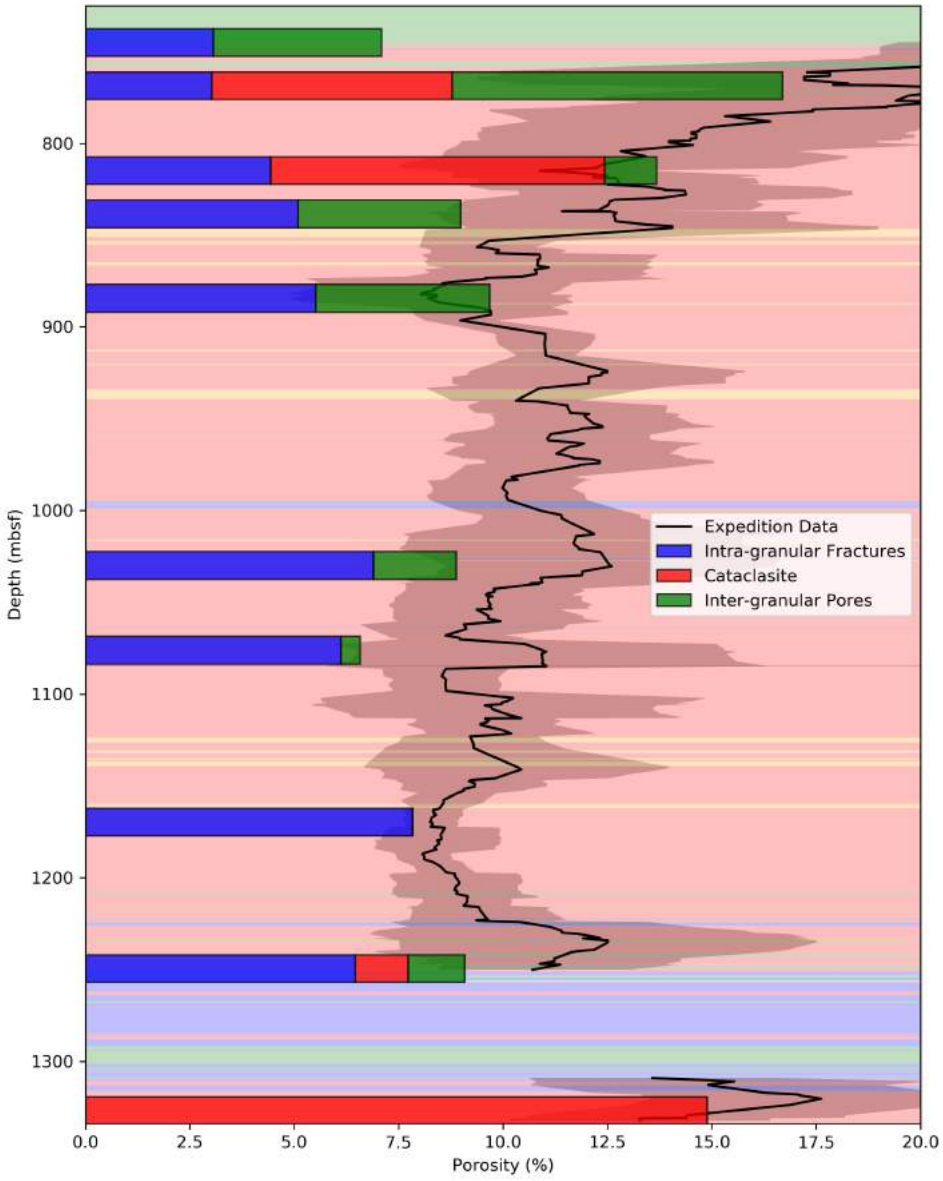

Figure 5. Porosities determined by SEM image analysis, subdivided by the type of porosity: intra-granular fractures, inter-granular pores, and cataclasites. Processed expedition data of porosity are shown for comparison. The black line is the moving average of the discrete sample measurements within a 12 m window, the grey envelope shows $\pm 1\sigma$ of the data within the window.

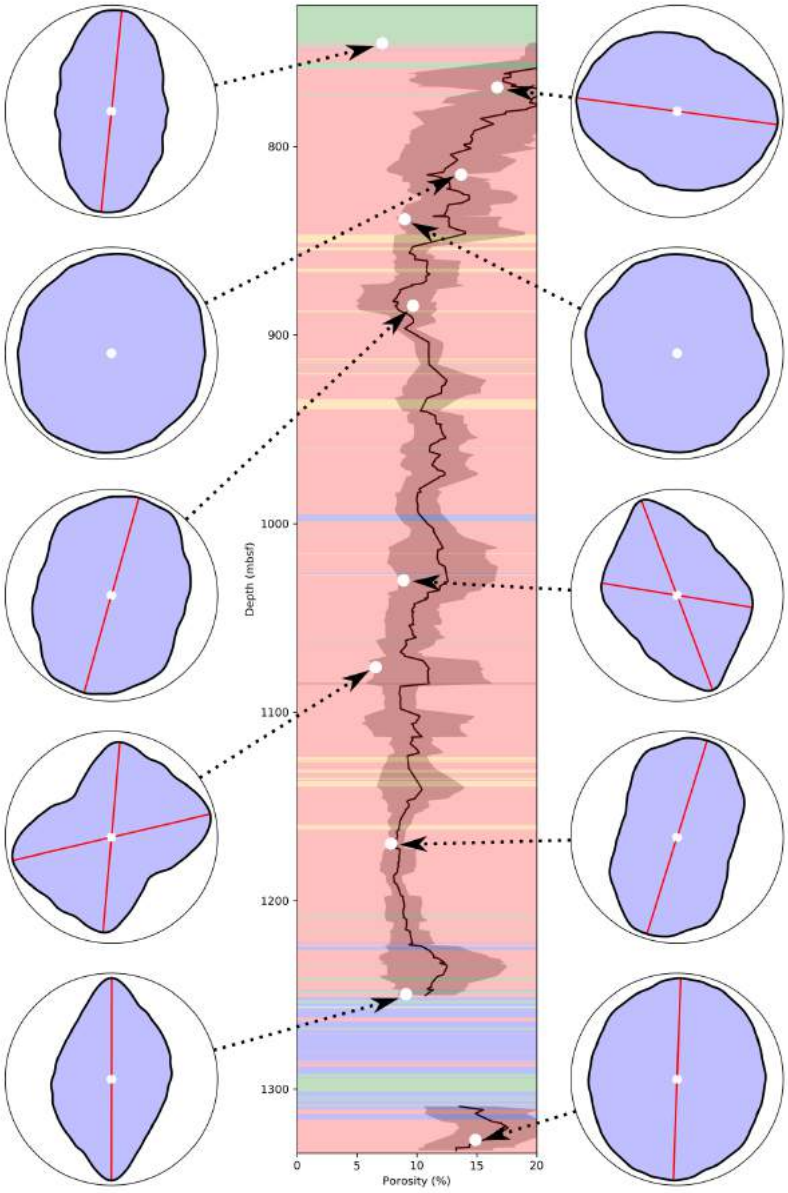

Figure 6. Pore orientation-frequency distributions for each of the analyzed thin sections. Orientations are measured as apparent dip, where upwards indicates a vertical apparent dip (i.e., 90°), while across indicates a horizontal apparent dip (i.e., 0°). Red lines indicate the mode(s) of the distributions. The central column shows the lithology, processed porosity measurements from Expedition 364, and, as white points, the porosities measured by SEM image analysis.

Table 1. Pore orientation distribution descriptions by sample. Most thin sections have uni- or bi-modal distributions. A qualitative indication of the relative peak height(s) is indicated in notes. The dominant overall orientation of pores in these samples is at apparent dips $> 69.4°$, with a sub-ordinate orientation at apparent dips $< 3.3°$.

Sample Name	Depth (mbsf)	Distribution Shape	Apparent Dip(s) (°)	Relative peak height
364-77-A-095-R-3-27-29	745.16	Unimodal	84.2	Strong
364-77-A-104-R-1-24-26	768.59	Unimodal	7.7	Moderate
364-77-A-121-R-1-75-77	814.85	Non-modal	—	—
364-77-A-132-R-1-22-24	838.45	Non-modal	—	—
364-77-A-150-R-1-53-55	884.43	Unimodal	74.3	Weak
364-77-A-204-R-1-07-09	1030.00	Bimodal	69.4 & 9.26	Strong & Moderate
364-77-A-219-R-1-22-24	1076.15	Bimodal	13.3 & 85.0	Strong & Strong
364-77-A-250-R-1-41-43	1169.71	Unimodal	72.7	Strong
364-77-A-276-R-1-17-19	1249.52	Unimodal	89.9	Strong
364-77-A-301-R-1-30-32	1326.89	Unimodal	88.0	Very Weak

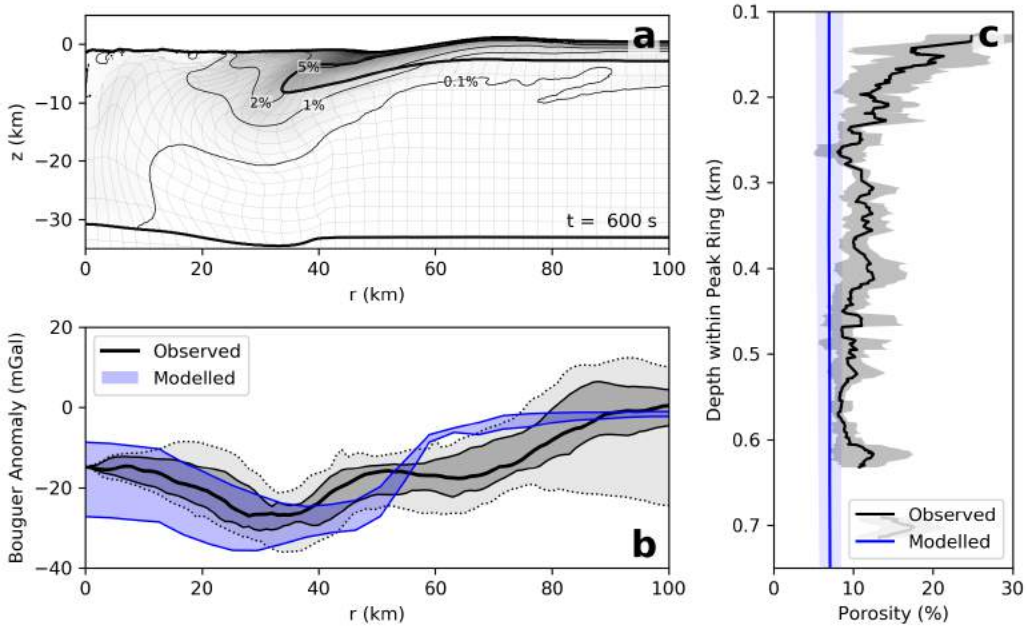

Figure 7. a) Porosity distribution at the end of the Chicxulub simulation. b) The modeled gravity anomaly (blue), based on setting the assigned reference density in the gravity calculation to the values in Table 2, compared to the observed gravity signal (black) of the Chicxulub structure (Figure 1b). c) The modeled porosity of Hole M0077A (blue) compared with porosity measurements (black) made during IODP-ICDP Expedition 364 (Figure 2).

ror. Overall, the modeled porosity closely matches the baseline values of porosity in the recovered core, with notable excursions within the top 200 m, from 300–350 m, and at 700 m within the peak ring. These excursions from the model may be caused by post-impact hydrothermal dissolution, and/or localisation of strain that is not captured by the model.

In addition to the simulated porosity in the peak ring, a set of simulated Bouguer gravity profiles of the crater were calculated from the iSALE simulation and are compared to the observed local Bouguer gravity anomaly (Figure 7b). The range in the displayed profiles results from propagating the uncertainties in the assigned reference densities for the materials in the model (Table 2).

One important problem with the calculation of the overall gravity profile comes from the filling of the basin with post-impact sedimentary rocks. In the model, the top of the peak ring is at 1050 m depth, while in the real crater, the top of the peak ring is at 618 mbsf. The cause of this discrepancy could be due to post-impact relaxation, or inaccuracies of the mechanism of transient weakening. To ensure that the mass-deficit from the post-impact sedimentary rocks is consistent with observations, one of two changes could be made: 1) The thickness of the sediments in the model could be maintained, but the reference density of the sedimentary infill increased such that the mass deficit remains constant, or 2) the reference density of post-impact sediments could be maintained at reasonable values but the thickness of the sedimentary infill reduced such that only 600 m of sedimentary rock overlie the peak ring. Here, we adopt the latter approach because it is more useful for predicting the gravity structure around the crater center. This approach will result in the model predicting a smaller magnitude anomaly in the terrace

zone compared to the observational data due to the lack of low-density sedimentary rock at those radial distances.

The modelled gravity signal possesses a mass deficit in the range of 5.81–9.25 × 10^{15} kg, considering the uncertainties presented in Table 2. This range includes the value of the mass deficit associated with the median gravity signal, 9.15 × 10^{15} kg, and is fully within the upper and lower quartile gravity signals. The maximum modelled anomaly at the crater center is -9 – -28 mGal, consistent with the observed value of ∼ -15 mGal. Additionally, the maximum anomaly in the modelled profile occurs between 28 and 40 km radial distance, and has a value of -22 – -34 mGal, consistent with the observed -26 mGal minimum at 35 km radial distance. Beyond the peak ring, within the annular trough and the terrace zone of the crater, the fit between the modelled and observed gravity profiles is poorer. This misfit can be explained primarily by the oversimplifications associated with modelling the post-impact sedimentary fill as a constant density material. The gravity anomaly is likely to be underestimated between 45–55 km radial distance, since deep sedimentary rocks in the annular trough adjacent to the peak ring are likely to have higher densities, as suggested by their increase in velocity with depth (Morgan et al., 2011). The overestimation of the observed profile from 55–75 km radial distance occurs, as previously stated, due to the lack of sedimentary infill at these radial distances. Additional causes of discrepancy between the model and observation may include: post-impact compaction, hydrothermal precipitation and/or dissolution, or a lack of initial porosity in the modelled pre-impact sedimentary rocks.

4 Discussion

The rocks of the Chicxulub peak ring, with porosities of 11.5 ± 4.7%, have low densities compared to typical crystalline basement rocks, which usually possess negligible porosity. Seismic velocities in the basement rocks of the region (Christeson et al., 2001) indicate that the pre-impact porosity of the crystalline target rocks was small, << 1%. Thus, compared to shocked target rocks in other craters (Pilkington & Grieve, 1992), the target rocks of the Chicxulub peak ring have among the highest impact-generated porosities of any impact structure (Table S4), i.e. almost all of the measured porosity in the crystalline rocks of the Chicxulub peak ring was produced by impact processes or post-impact alteration. We attribute the remarkably high porosity to the relative size and age of the Chicxulub impact, sampling depth within the structure, and the complex deformation path that peak ring materials follow during dynamic collapse (Rae et al., 2019).

The main contributor to the porosity of target rocks in the Chicxulub impact structure is shock-induced micro-fracturing. Additional porosity is contributed from cataclasites, which are extremely porous but volumetrically small, and, possibly, large inter-granular pores. The origin of large inter-granular pores is almost certainly due to preparation-induced damage. Nevertheless, large inter-granular pores are systematically prevalent near the top of the granitic rock section, coinciding with the largest deviation between the modeled porosity and observed porosity.

Most peak-ring material never experiences tensile stress regimes during cratering (Rae et al., 2019). Consequently, the shear-induced dilatancy model used here should simulate the production of all styles of primary micro-porosity observed within the peak ring rocks. Secondary porosity may be generated by processes such as hydrothermal dissolution. The observational evidence shows that the porosity of the peak ring rocks is primarily hosted in intra-granular fractures formed by shock metamorphism. In contrast, the dilatancy model predicts that very minimal amounts of porosity are produced during the passage of the shock wave and rarefaction. Instead it predicts that, for the shallowest rocks in the peak ring, porosity is generated in two distinct phases of shear deformation, the first during transient cavity formation and rim collapse (0–100 s) and the

Table 2. Range of target material densities used in gravity calculation.

Material	Selected Reference Density (kg m^{-3})	Reported Density (kg m^{-3})	Reference
Pre-impact Sedimentary Rock	2650 ± 50	2477–2938	Elbra and Pesonen (2011)
Crystalline Basement	2628 ± 39	2628 ± 39	This study & Christeson et al. (2018)
Mantle	3320	3320	Benz et al. (1989)
Post-impact Sedimentary Rock*	2200 ± 50	1960–2470	Christeson et al. (2018)
Bouguer Density	2670	2670	Tanner et al. (1988)

*The thickness of post-impact sedimentary rocks above the peak ring was maintained at 650 m

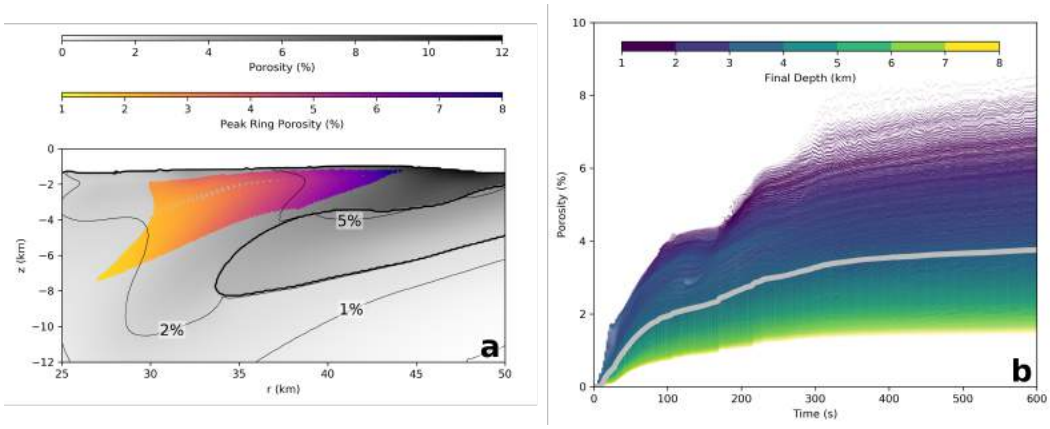

Figure 8. The distribution of porosity within the Chicxulub peak ring, and the timing of its generation. a) Porosity distribution at the final timestep, focussed upon the peak ring. Slumped sedimentary rocks beneath the peak ring are distinguished from crystalline rocks by a thick black line, while thin black lines show contours of porosity. Peak ring material is highlighted by the coloured points. b) Porosity of peak ring material through time, coloured by the material's final depth. The grey line is a mass-weighted average of porosity in the peak ring through time.

second during central peak formation and collapse (175–350 s) (Figure 8b). Deeper material within the peak ring structure experiences only one distinct phase of shear-induced dilatancy, which occurs more gradually through transient cavity formation and collapse. One explanation for the discrepancy between the observation of shock-induced microfractures dominating porosity and the model prediction of later porosity generation by shear is that fractures form early, during high pressure shock, without any porosity. Those fractures must then open during later shear-dominated phases of crater deformation. However, it is also possible that the shear-induced dilatancy model used here is an oversimplification of the process that generates porosity in para-autochthonous impactites. A process that may involve two distinct stages of porosity-generation; first, a dynamic effect of fracturing during shock, and the second due to true shear-induced dilatancy of a pre-damaged material. If this is the case, the GSI parameters used here for shear-induced dilatancy are too large.

The ability to accurately predict the porosity distribution of complex craters is important for understanding the gravity signal of large impact structures. Here, we have obtained a reasonable fit to the observed gravity signature of the Chicxulub structure, a large complex impact crater, using a numerical model that accounts for porosity generation/density reduction by dilatancy alone. Discrepancies between the modeled and observed gravity signals may be due to pore-space compaction or displacement of pre-existing crustal density variations not captured by the model. Additionally, changes to acoustic fluidisation parameters may change the location of down-faulted sedimentary rocks in the collapsed transient cavity rim that underlies the peak ring, and therefore affect the modeled gravity signature. Despite this, the overall consistency between the gravity profiles and porosities between observation and model reinforces the significance of dilatancy on sub-crater structure and deformation. Additionally, our results support the recommendation by Collins (2014), that low GSI dilatancy parameters should be used for impact cratering simulations.

4.1 Orientation of Micro-Fractures

In addition to the consistency between porosity and gravity measurements with the results of numerical impact simulations, it is also possible to predict the orientation of shock-induced micro-fractures in numerical impact simulations (Rae et al., 2019). Predicting the orientation of micro-fractures during cratering requires the assumption of two well-accepted concepts of shock physics and rock mechanics. Firstly, the orientation of fractures during rock failure is predicted by the canonical model of Mohr-Coulomb rock failure (Anderson, 1905). In low-pressure regimes, rock failure is typically expected at 30° to the orientation of σ_1, depending on the coefficient of internal friction. However, in a high-pressure regime, greater than the Hugoniot Elastic Limit (HEL), the coefficient of internal friction approaches zero, and consequently, the angle of failure approaches 45° to σ_1. Secondly, the formation of PFs during shock occurs during shock loading, i.e., once the HEL is exceeded but before peak pressure conditions are reached (French & Koeberl, 2010; Poelchau & Kenkmann, 2011). Support for this assertion derives from the observation that PFs commonly separate domains within grains that Planar Deformation Features (PDFs), which are sensitive to the peak pressure of the shock wave, do not cross. Using these concepts, and by obtaining the orientations and magnitudes of deviatoric principal stresses, following the methodology described by Rae et al. (2019), it is possible to predict shock fracture orientations within target material during shock (Figure 9).

During crater excavation and modification, and to a much lesser extent, during shock, material is expected to rotate from its initial orientation. The orientation of material in numerical simulations can be tracked by calculation of infinitesimal strain tensors (See Rae et al. (2019)). Here, the Dynamic Collapse Model has been used, and a single tracer selected to represent the recovered core material. This particle rotates by approximately 60° clockwise during cratering (Figure 10c). Selecting tracers from deeper, or at increasing radial distances within the peak ring material, causes a systematic increase in the total clockwise rotation during cratering by up to an additional 30°. Consequently, the final orientation of shock-related fractures, as predicted by the model, is at concentric strikes, dipping at 88° inwards –78° outwards, and the conjugate set at 12° inwards – 2° outwards (Figure 10b). The observed orientations of micro-fractures within the shocked granitic rock samples can be sub-divided into one set of steep apparent dips (69.4–89.9°) and a second set with shallow apparent dips (7.7–13.3°). Despite the observations only being capable of determining apparent dip, without any strike information, the modeled orientations are remarkably consistent with the observed micro-fracture orientations.

This result indicates several important points. Firstly, that the orientation at which shock micro-fractures, i.e. PFs, form may be primarily controlled by the orientation of principal stresses during shock. The granitic rocks from Hole M0077A have minimal to no grain preferred orientation (Morgan et al., 2017; Riller et al., 2018); consequently, the preferred orientation of shock micro-fractures across a whole thin section of randomly oriented grains indicates that crystallographic orientation may not have primary control of the orientation of fractures. PFs are known to form on rational crystallographic planes (French & Koeberl, 2010); however, it is likely that the specific orientation of the plane that is activated during shock may be controlled by stress conditions.

Secondly, it is clear that a large rotation of the peak ring material is required between shock and the final emplacement of the peak ring. Regardless of the physical mechanism by which crater collapse occurs, the orientation of fractures due to shock will always be at moderate dip angles (approximately 45°) immediately after shock. Achieving conjugate sets of planar fractures in sub-vertical and sub-horizontal respective orientations requires either a clockwise rotation of material by approximately 60–70° or an anti-clockwise rotation of 20–30°. The Dynamic Collapse Model of peak-ring formation precisely predicts the large clockwise rotation required.

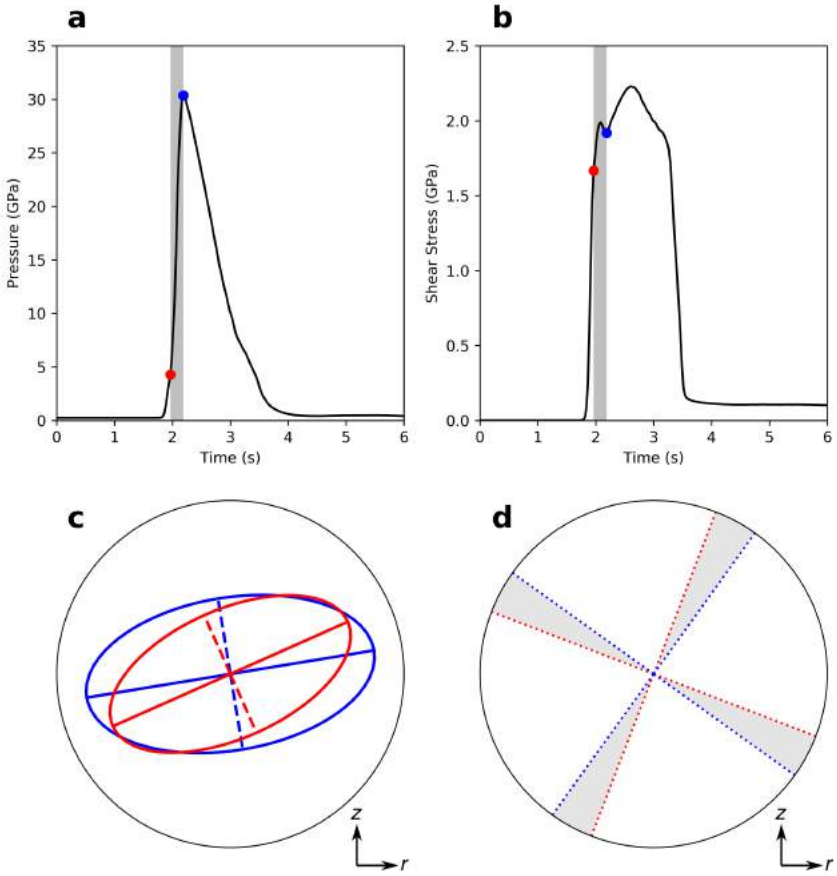

Figure 9. Fracture formation during shock. a) and b) Pressure and maximum resolvable shear stress, respectively, during shock. PF formation is expected to occur between the time at which the HEL is exceeded (red), and the time of maximum pressure (blue). c) Cross-sections of the Lamé deviatoric stress ellipsoid are shown at the times corresponding to the time points. Solid lines within the ellipses indicate the orientation and relative magnitude of the maximum deviatoric principle stress, dashed lines within the ellipses indicate the orientation and relative magnitude of the minimum deviatoric principle stress. d) PF formation is expected at 45° to the orientation of σ_1, therefore PFs are expected to form at orientations within the grey areas. (Note: the highlighted grey areas take into account the rotation of the tracer particle by roughly 1° anti-clockwise during shock).

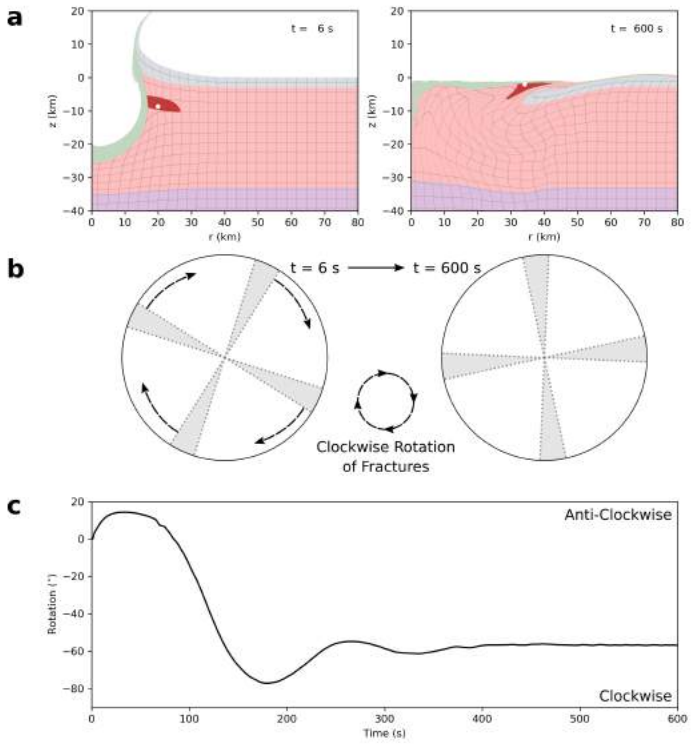

Figure 10. Rotation of micro-fractures during modification. a) Arrangement of the crater after shock passage and crater modification. Peak ring material is highlighted by the red material while the individual tracer being tracked is highlighted by the white point. b) Orientation of shock micro-fractures at the timesteps indicated. c) Cumulative orientation of the selected tracer particle throughout all timesteps of the simulation.

Finally, stress-induced fractures significantly affect the permeability anisotropy of rocks. Canonically, the maximum permeability direction of a fault rock is along the intersection of minor-faults, i.e., parallel to the orientation of the σ_2 direction that produced the fractures (Sibson, 2000). Combining this with the fact that shock micro-fracturing produces the dominant pore fabric in these peak ring rocks leads to possibility that numerical impact simulations may be able to predict the permeability distribution and anisotropy within impact craters, a critical parameter of hydrothermal models of impact structures.

5 Conclusions

Here, we have shown that the unusually high porosities of the Chicxulub peak-ring reported by Morgan et al. (2016, 2017) and Christeson et al. (2018) are caused by pervasive, shock-induced microfracturing. The present-day orientation of the shock microfractures are consistent with predictions of the Dynamic Collapse Model of peak-ring formation regarding the orientation of principal stresses during shock and the subsequent deformation of material during crater collapse. An important implication of this work is that PFs in quartz could be sensitive to the orientation of principal stresses during shock. In turn, this suggests that porosity and permeability is likely to be anisotropic throughout craters. Finally, the results presented in this contribution demonstrate that the dilatancy model of Collins (2014) produces predictions of the porosities of peak-ring rocks and the gravity anomaly across the entire structure that are remarkably consistent with petrophysical and remote geophysical observations. This provides a simple gravity model of the Chicxulub structure that accounts for all of the important processes that generate mass deficits within craters.

Appendix A Expedition 364 Scientists

S. P. S. Gulick[1,2], J. V. Morgan[3], E. Chenot[4], G. L. Christeson[2], P. Claeys[5], C. S. Cockell[6], M. J. L. Coolen[7], L. Ferrière[8], C. Gebhardt[9], K. Goto[10], S. Green[11], H. Jones[12], D. A. Kring[13], J. Lofi[4], C. M. Lowery[2], R. Ocampo-Torres[14], L. Perez-Cruz[15], A. E. Pickersgill[16, 17], M. Poelchau[18], A. S. P. Rae[2], C. Rasmussen[4,19], M. Rebolledo-Vieyra[20], U. Riller[21], H. Sato[22], J. Smit[23], S. M. Tikoo[24], N. Tomioka[25], J. Urrutia-Fucugauchi[15], M. T. Whalen[26], A. Wittmann[27], L. Xiao[28], K. E. Yamaguchi[29, 30].

[1]Department of Geological Sciences, Jackson School of Geosciences, University of Texas at Austin, Austin, TX, USA. [2]Institute for Geophysics, Jackson School of Geosciences, University of Texas at Austin, Austin, TX, USA. [3]Department of Earth Science and Engineering, Imperial College London, London, UK. [4]Géosciences Montpellier, Université de Montpellier, Montpellier, France. [5]Analytical, Environmental and Geo-Chemistry, Vrije Universiteit Brussel, Brussels, Belgium. [6]Centre for Astrobiology, School of Physics and Astronomy, University of Edinburgh, Edinburgh, UK. [7]Western Australia Organic and Isotope Geochemistry Centre (WA-OIGC), School of Earth and Planetary Sciences, Curtin University, Bentley, WA 6102, Australia. [8]Natural History Museum, Vienna, Austria. [9]Alfred Wegener Institute Helmholtz Centre of Polar and Marine Research, Bremerhaven, Germany. [10]Department of Earth and Planetary Science, University of Tokyo, Tokyo, Japan. [11]British Geological Survey, Edinburgh, UK. [12]Department of Geosciences, Pennsylvania State University, University Park, PA, USA. [13]Lunar and Planetary Institute, Houston, TX, USA. [14]Groupe de Physico-Chimie de l'Atmosphère, L'Institut de Chimie et Procédés pour l'Énergie, l'Environnement et la Santé (ICPEES), Université de Strasbourg, Strasbourg, France. [15]Instituto de Geofísica, Universidad Nacional Autónoma De México, Ciudad De México, Mexico. [16]School of Geographical and Earth Sciences, University of Glasgow, Glasgow, UK. [17]Argon Isotope Facility, Scottish Universities Environmental Research Centre, East Kilbride, UK. [18]Department of Geology, University of Freiburg, Freiburg, Germany. [19]Department of Geology and Geophysics, University of Utah, Salt Lake City, UT, USA. [20]Independent consultant, Cancun, Mexico. [21]Institut

für Geologie, Universität Hamburg, Hamburg, Germany. [22]Japan Agency for Marine-Earth Science and Technology, Kanagawa, Japan. [23]Faculty of Earth and Life Sciences (FALW), Vrije Universiteit Amsterdam, Amsterdam, Netherlands. [24]Earth and Planetary Sciences, Rutgers University, New Brunswick, NJ, USA. [25]Kochi Institute for Core Sample Research, Japan Agency for Marine-Earth Science and Technology, Kochi, Japan. [26]Department of Geosciences, University of Alaska Fairbanks, Fairbanks, AK, USA. [27]Eyring Materials Center, Arizona State University, Tempe, AZ, USA. [28]School of Earth Sciences, Planetary Science Institute, China University of Geosciences, Wuhan, China. [29]Department of Chemistry, Toho University, Chiba, Japan. [30]NASA Astrobiology Institute.

Appendix B Author Contributions

The work in this contribution was carried out during the PhD research of ASPR. The PhD project was planned and supervised by JVM, GSC, RAFG, and GRO. SEM images were acquired by ASPR and TS. JLe carried out some of the image processing and analysis as part of a Masters project supervised by ASPR and JVM. ASPR, GC, CG, and JLo contributed to the acquisition of petrophysical data during IODP-ICDP Expedition 364. ASPR carried out the iSALE numerical simulations and post-processing of the results. ASPR wrote the first draft and all authors contributed to subsequent drafts.

Appendix C Data availability

Data from IODP-ICDP Expedition 364 is available upon request from `http://iodp.pangaea.de/`. Gravity data, courtesy of Alan Hildebrand and Mark Pilkington, is available available as a supplementary data file, along with the gravity profile determined in this study. iSALE is not a publicly available code, however, depending on usage terms, access is available upon request of the lead developers. Details of iSALE access are available at `www.isale-code.de`.

Acknowledgments

We gratefully acknowledge the developers of iSALE, including Kai Wünnemann, Dirk Elbeshausen, Boris Ivanov and Jay Melosh. Some plots in this work were created with the pySALEPlot tool written by Tom Davison. We gratefully acknowledge 2 anonymous reviewers and the associate editor for their constructive criticism. The Chicxulub drilling expedition was funded by the IODP as Expedition 364 with co-funding from the ICDP. Expedition 364 was implemented by ECORD, with contributions and logistical support from the Yucatán state government and UNAM. The work presented here was funded by STFC (ST/N000803/1) and NERC (NE/P011195/1), additional support was received from NSF-OCE-1737351. This is UTIG Contribution #XXXX.

References

Abramov, O., & Kring, D. (2007). Numerical modeling of impact-induced hydrothermal activity at the Chicxulub crater. *Meteoritics & Planetary Science*, *42*(1), 93–112. doi: 10.1111/j.1945-5100.2007.tb00220.x

Amsden, A., Ruppel, H., & Hirt, C. (1980). *SALE: A simplified ALE computer program for fluid flow at all speeds.* (Tech. Rep. No. LA-8095). New Mexico: Los Alamos National Laboratories.

Anderson, E. (1905). The dynamics of faulting. *Transactions of the Edinburgh Geological Society*, *8*(3), 387–402. doi: 10.1144/transed.8.3.387

Benz, W., Cameron, A., & Melosh, H. (1989). The origin of the Moon and the single-impact hypothesis III. *Icarus*, *81*(1), 113–131. doi: 10.1016/0019-1035(89)90129-2

Campos-Enriquez, J., MoralesRodríguez, H., DomínguezMendez, F., & Birch, F. (1998). Gausss theorem, mass deficiency at Chicxulub crater (Yucatan, Mexico), and the extinction of the dinosaurs. *Geophysics*, *63*(5), 1585–1594. doi: 10.1190/1.1444455

Christeson, G., Collins, G., Morgan, J., Gulick, S., Barton, P., & Warner, M. (2009). Mantle deformation beneath the Chicxulub impact crater. *Earth and Planetary Science Letters*, *284*(12), 249–257. doi: 10.1016/j.epsl.2009.04.033

Christeson, G., Gulick, S., Morgan, J., Gebhardt, C., Le Ber, E., Lofi, J., ... W. Zylberman (2018). Extraordinary Rocks of the Chicxulub Crater Peak-ring: Physical Property Measurements from IODP/ICDP Expedition 364. *Earth and Planetary Science Letters*, *495*, 1-11.

Christeson, G., Nakamura, Y., Buffler, R. T., Morgan, J., & Warner, M. (2001). Deep crustal structure of the chicxulub impact crater. *Journal of Geophysical Research: Solid Earth*, *106*(B10), 21751–21769.

Cockell, C. (2006). The origin and emergence of life under impact bombardment. *Philosophical Transactions of the Royal Society of London B: Biological Sciences*, *361*(1474), 1845–1856. doi: 10.1098/rstb.2006.1908

Collins, G. (2014). Numerical simulations of impact crater formation with dilatancy. *Journal of Geophysical Research: Planets*, *119*(12), 2600–2619. doi: 10.1002/2014JE004708

Collins, G., Melosh, H., Morgan, J., & Warner, M. (2002). Hydrocode Simulations of Chicxulub Crater Collapse and Peak-Ring Formation. *Icarus*, *157*(1), 24–33. doi: 10.1006/icar.2002.6822

Collins, G., Morgan, J., Barton, P., Christeson, G., Gulick, S., Urrutia, J., ... Wünnemann, K. (2008). Dynamic modeling suggests terrace zone asymmetry in the Chicxulub crater is caused by target heterogeneity. *Earth and Planetary Science Letters*, *270*(34), 221–230. doi: 10.1016/j.epsl.2008.03.032

Elbra, T., & Pesonen, L. (2011). Physical properties of the Yaxcopoil-1 deep drill core, Chicxulub impact structure, Mexico. *Meteoritics & Planetary Science*, *46*(11), 1640–1652. doi: 10.1111/j.1945-5100.2011.01253.x

Espindola, J., Mena, M., de La Fuente, M., & Campos-Enriquez, J. (1995). A model of the Chicxulub impact structure (Yucatan, Mexico) based on its gravity and magnetic signatures. *Physics of the Earth and Planetary Interiors*, *92*(3), 271–278. doi: 10.1016/0031-9201(95)03022-6

French, B., & Koeberl, C. (2010). The convincing identification of terrestrial meteorite impact structures: What works, what doesn't, and why. *Earth-Science Reviews*, *98*(12), 123–170. doi: 10.1016/j.earscirev.2009.10.009

Grieve, R. (2005). Economic natural resource deposits at terrestrial impact structures. *Geological Society, London, Special Publications*, *248*(1), 1–29. doi: 10.1144/GSL.SP.2005.248.01.01

Grieve, R., Robertson, P., & Dence, M. (1981). Constraints on the formation of ring impact structures, based on terrestrial data. In *Multi-ring basins: Formation and evolution* (pp. 37–57).

Gulick, S., Barton, P., Christeson, G., Morgan, J., McDonald, M., Mendoza-Cervantes, K., ... Warner, M. (2008). Importance of pre-impact crustal structure for the asymmetry of the Chicxulub impact crater. *Nature Geoscience*, *1*(2), 131–135. doi: 10.1038/ngeo103

Gulick, S., Christeson, G., Barton, P., Grieve, R., Morgan, J., & Urrutia-Fucugauchi, J. (2013). Geophysical Characterization of the Chicxulub Impact Crater. *Reviews of Geophysics*, *51*(1), 31–52. doi: 10.1002/rog.20007

Hildebrand, A., Penfield, G., Kring, D., Pilkington, M., Camargo, A., Jacobsen, S., & Boynton, W. (1991). Chicxulub Crater: A possible Cretaceous/Tertiary boundary impact crater on the Yucatán Peninsula, Mexico. *Geology*, *19*(9), 867–871. doi: 10.1130/0091-7613(1991)019⟨0867:CCAPCT⟩2.3.CO;2

Hildebrand, A., Pilkington, M., Connors, M., Ortiz-Aleman, C., & Chavez, R.

(1995). Size and structure of the Chicxulub crater revealed by horizontal gravity gradients and cenotes. *Nature*, *376*(6539), 415. doi: 10.1038/376415a0

Ivanov, B. (2005). Numerical Modeling of the Largest Terrestrial Meteorite Craters. *Solar System Research*, *39*(5), 381–409. doi: 10.1007/s11208-005-0051-0

Ivanov, B., Deniem, D., & Neukum, G. (1997). Implementation of dynamic strength models into 2d hydrocodes: Applications for atmospheric breakup and impact cratering. *International Journal of Impact Engineering*, *17*(15), 375–386. doi: 10.1016/S0734-743X(97)87511-2

Kring, D., Kramer, G., Collins, G., Potter, R., & Chandnani, M. (2016). Peak-ring structure and kinematics from a multi-disciplinary study of the schrödinger impact basin. *Nature communications*, *7*, 13161.

Melosh, H. (1989). *Impact cratering: A geologic process* (No. 11). New York: Oxford University Press.

Melosh, H., Ryan, E., & Asphaug, E. (1992). Dynamic fragmentation in impacts: Hydrocode simulation of laboratory impacts. *Journal of Geophysical Research: Planets*, *97*(E9), 14735–14759. doi: 10.1029/92JE01632

Morgan, J., Gulick, S., Bralower, T., Chenot, E., Christeson, G., Claeys, P., ... Zylberman, W. (2016). The formation of peak rings in large impact craters. *Science*, *354*(6314), 878–882. doi: 10.1126/science.aah6561

Morgan, J., Gulick, S., Mellet, C., Green, S., & Expedition 364 Scientists. (2017). *Chicxulub: Drilling the K-Pg Impact Crater* (Vol. 364). International Ocean Discovery Program. doi: 10.14379/iodp.proc.364.2017

Morgan, J., Warner, M., Collins, G., Grieve, R., Christeson, G., Gulick, S., & Barton, P. (2011). Full waveform tomographic images of the peak ring at the chicxulub impact crater. *Journal of Geophysical Research: Solid Earth*, *116*(B6).

Morgan, J., Warner, M., Collins, G., Melosh, H., & Christeson, G. (2000). Peak-ring formation in large impact craters: geophysical constraints from Chicxulub. *Earth and Planetary Science Letters*, *183*(34), 347–354. doi: 10.1016/S0012-821X(00)00307-1

Morgan, J., Warner, M., the Chicxulub Working Group, Brittan, J., Buffler, R., Camargo, A., ... Trejo, A. (1997). Size and morphology of the Chicxulub impact crater. *Nature*, *390*(6659), 472–476. doi: 10.1038/37291

Penfield, G., & Camargo, Z. (1981). Definition of a major igneous zone in the central yucatan platform with aeromagnetics and gravity. *Technical program, abstracts and biographies (Society of Exploration Geophysicists 51st annual international meeting): Los Angeles, Society of Exploration Geophysicists*, 37.

Pilkington, M., & Grieve, R. (1992). The geophysical signature of terrestrial impact craters. *Reviews of Geophysics*, *30*(2), 161–181. doi: 10.1029/92RG00192

Pilkington, M., Hildebrand, A., & Ortiz-Aleman, C. (1994). Gravity and magnetic field modeling and structure of the Chicxulub Crater, Mexico. *Journal of Geophysical Research: Planets*, *99*(E6), 13147–13162. doi: 10.1029/94JE01089

Poelchau, M., & Kenkmann, T. (2011). Feather features: A low-shock-pressure indicator in quartz. *Journal of Geophysical Research: Solid Earth*, *116*(B2), B02201. doi: 10.1029/2010JB007803

Rae, A., Collins, G., Poelchau, M., Riller, U., Davison, T., Grieve, R., ... IODP-ICDP Expedition 364 Scientists (2019). Stress-Strain Evolution during Peak-Ring Formation: A Case Study of the Chicxulub Impact Structure. *Journal of Geophysical Research: Planets*, *124*(2), 396–417.

Riller, U., Poelchau, M. H., Rae, A. S. P., Schulte, F. M., Collins, G. S., Melosh, H. J., ... IODP-ICDP Expedition 364 Science Party (2018). Rock fluidization during peak-ring crater formation. *Nature*, *562*(7728), 511. doi: 10.1038/s41586-018-0607-z

Schindelin, J., Arganda-Carreras, I., Frise, E., Kaynig, V., Longair, M., Pietzsch, T., ... Cardona, A. (2012). Fiji: an open-source platform for biological-image

764 analysis. *Nature Methods*, *9*(7), 676–682. doi: 10.1038/nmeth.2019
765 Sharpton, V. L., Burke, K., Camargo-Zanoguera, A., Hall, S. A., Lee, D. S., Marn,
766 L. E., ... Urrutia-Fucugauchi, J. (1993). Chicxulub Multiring Impact Basin:
767 Size and Other Characteristics Derived from Gravity Analysis. *Science*,
768 *261*(5128), 1564–1567. doi: 10.1126/science.261.5128.1564
769 Sharpton, V. L., Marin, L. E., Carney, J. L., Lee, S., Ryder, G., Schuraytz, B. C.,
770 ... Spudis, P. D. (1996). A model of the Chicxulub impact basin based on
771 evaluation of geophysical data, well logs, and drill core samples. In G. Ryder,
772 D. Fastovsky, & S. Gartner (Eds.), *The Cretaceous-Tertiary Event and Other*
773 *Catastrophes in Earth History, Spec. Pap. 307* (pp. 55–74). Boulder, CO:
774 Geological Society of America.
775 Sibson, R. H. (2000). Fluid involvement in normal faulting. *Journal of Geodynamics*,
776 *29*(3), 469–499. doi: 10.1016/S0264-3707(99)00042-3
777 Tanner, J., Aiken, C., Dehlinger, P., Dewhurst, W., de la Fuente, M., Godley, V., ...
778 Thorning, L. (1988). Gravity Anomaly Map of North America. *The Leading*
779 *Edge*, *7*(11), 15–18. doi: 10.1190/1.1439456
780 Vermeesch, P. M., Morgan, J. V., Christeson, G. L., Barton, P. J., & Surendra, A.
781 (2009). Three-dimensional joint inversion of traveltime and gravity data across
782 the Chicxulub impact crater. *Journal of Geophysical Research: Solid Earth*,
783 *114*(B2), B02105. doi: 10.1029/2008JB005776
784 Winkler, R., Luther, R., Poelchau, M. H., Wünnemann, K., & Kenkmann, T.
785 (2018). Subsurface deformation of experimental hypervelocity impacts in
786 quartzite and marble targets. *Meteoritics & Planetary Science*, *53*(8), 1733–
787 1755. doi: 10.1111/maps.13080
788 Wünnemann, K., Collins, G. S., & Melosh, H. J. (2006). A strain-based poros-
789 ity model for use in hydrocode simulations of impacts and implications for
790 transient crater growth in porous targets. *Icarus*, *180*(2), 514–527. doi:
791 10.1016/j.icarus.2005.10.013
792 Zuber, M. T., Smith, D. E., Watkins, M. M., Asmar, S. W., Konopliv, A. S.,
793 Lemoine, F. G., ... Yuan, D.-N. (2013). Gravity Field of the Moon from
794 the Gravity Recovery and Interior Laboratory (GRAIL) Mission. *Science*,
795 *339*(6120), 668–671. doi: 10.1126/science.1231507

Impact-induced Porosity and Micro-fracturing at the Chicxulub Impact Structure — Supplementary Material

Auriol S. P. Rae[1,2], Gareth S. Collins[1], Joanna V. Morgan[1], Tobias Salge[3], Gail L. Christeson[4], Jody Leung[1], Johanna Lofi[5], Sean P. S. Gulick[4], Michael Poelchau[2], Ulrich Riller[6], Catalina Gebhardt[7], Richard A. F. Grieve[8], Gordon R. Osinski[8], IODP-ICDP Expedition 364 Scientists

[1]Department of Earth Science and Engineering, Imperial College London, London, UK, SW7 2BP

[2]Institut für Geo- und Umweltnaturwissenschaften, Albert-Ludwigs-Universität Freiburg, Geologie, 79104 Freiburg, Germany

[3]Imaging and Analysis Centre, Natural History Museum, London, UK, SW7 5BD

[4]Institute for Geophysics and Department of Geological Sciences, Jackson School of Geosciences, University of Texas at Austin, Austin, TX, USA

[5]Gèosciences Montpellier, Universitè de Montpellier, Montpellier, France

[6]Institut für Geologie, Universität Hamburg, Bundesstrasse 55, 20146 Hamburg, Germany

[7]Alfred Wegener Institute Helmholtz Centre of Polar and Marine Research, Bremerhaven, Germany.

[8]Department of Earth Sciences / Centre for Planetary Science and Exploration, Western University, London, Ontario, N6A 3K7, Canada

Contents

Corresponding author: Auriol S. P. Rae, auriol.rae@geologie.uni-freiburg.de

1 Observational Data

In this section of Supplementary Material, we show supplementary observational data. First, we show a schematic log, Bouguer gravity map, and location of IODP-IDCP Expedition 364 Hole M0077A (Figure S1). Furthermore, we show the results of determining the average radial gravity profile of the Chicxulub crater without removing anomalous regions to the north-west and south of the crater center (Figure S2), in addition, the average gravity profile (excluding the anomalous regions) calculated during this work can be found as a Supplementary Data File. Thirdly, we show unprocessed petrophysical data from IODP-ICDP Expedition 364 (Figure S3). The data itself can be obtained from from `http://iodp.pangaea.de/`. Finally, this section of the Supplementary Material contains additional information on the back-scattered electron (BSE) scanning electron microscope (SEM) images obtained during this work (Table S1), and low resolution versions of all the stitched SEM images, with pore size-frequency distributions and histograms of pore orientation (Figures S4-S13). Here, the term "pore size" refers to the square root of the area of the pore, thus indicating the area of the pore in terms of a one-dimensional approximation of the diameter of the pore. Finally, we show an example image that compares a stitched SEM image to the orientation of pores thresholded in ImageJ (Figure S14).

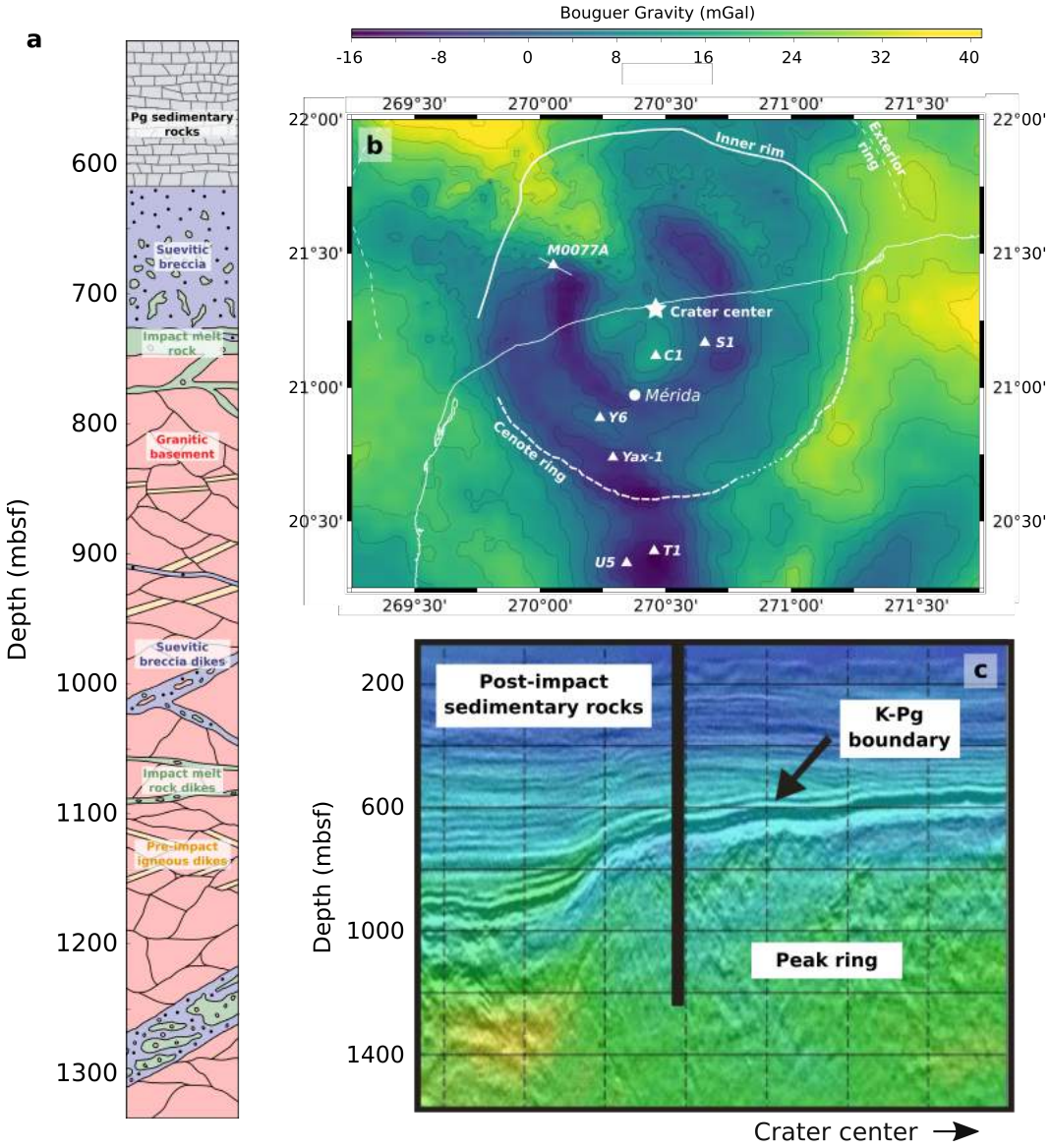

Figure S1. a) Schematic stratigraphic log of Hole M0077A. The location of M0077A is indicated on subfigures b) and c). b) A Bouguer gravity map of the crater. Gravity data are contoured at 5 mGal intervals. Additionally, the seismically mapped Inner Rim and Exterior Ring are indicated offshore, while the Cenote Ring is indicated onshore. Finally, the locations of the crater center, the city of Mérida, and some previous drill sites (C1 — Chicxulub-1, S1 — Sacapuc-1, Y6 — Yucatán-6, Yax-1 — Yaxcopoil-1, T1 — Ticul-1, and U5 — UNAM-5) are indicated. c) A radial seismic profile and velocity model across the peak ring through the site location and of length indicated on b). Gravity data courtesy of A. Hildebrand and M. Pilkington. After *Rae et al.* (2019), adapted from *Gulick et al.* (2013) and *Morgan et al.* (2016).

Table S1. List of images and their specifications, images are available upon request of the authors.

Sample Name	Depth (mbsf)	Description	Image Dimensions (pixels)	Pixels (MP)	Pixel Resolution (nm)	Image Area (mm^2)
364-77-A-095-R-3-27-29	745.16	Fractured Granite	33910 × 26554	900.4	748.9	505.0
364-77-A-104-R-1-24-26	768.59	Fractured Granite with cataclasite veins	25704 × 31968	821.7	748.9	460.9
364-77-A-121-R-1-75-77	814.85	Fractured Granite with cataclasite veins	34136 × 26318	898.4	748.9	503.8
364-77-A-132-R-1-22-24	838.45	Fractured Granite	42776 × 22319	945.7	748.9	530.4
364-77-A-150-R-1-53-55	884.43	Fractured Granite	41873 × 23925	1001.8	748.9	561.7
364-77-A-204-R-1-07-09	1030.00	Fractured Granite	32108 × 21090	677.2	748.9	379.8
364-77-A-219-R-1-22-24	1076.15	Fractured Granite	33880 × 21418	725.6	748.9	407.0
364-77-A-250-R-1-41-43	1169.71	Fractured Granite	41836 × 18912	791.2	748.9	443.7
364-77-A-276-R-1-17-19	1249.52	Fractured Granite with cataclasite veins	38664 × 21240	821.2	748.9	460.6
364-77-A-301-R-1-30-32	1326.89	Granitic Breccia	35982 × 22582	812.5	748.9	455.7

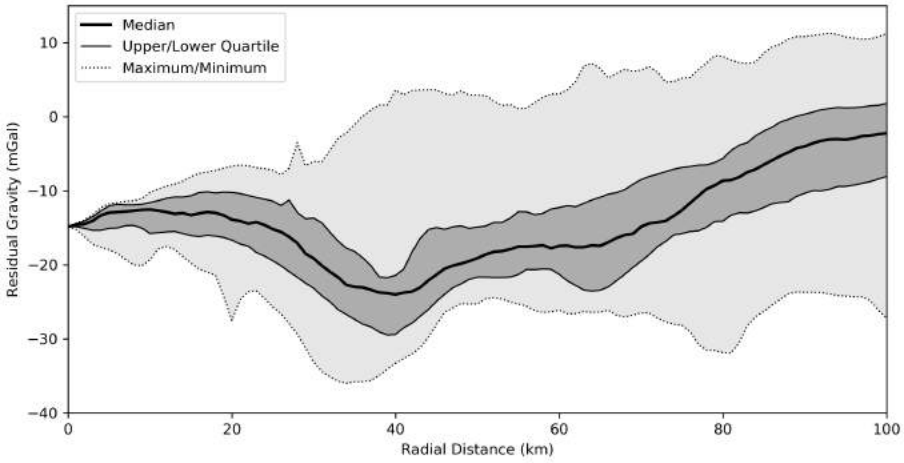

Figure S2. Average (median) radial gravity profile of the Chicxulub structure, including data from all azimuths. Upper and lower quartiles, and minimum and maximum values are indicated. See Figure 1b to compare with the profile made with data excluded in anomalous regions.

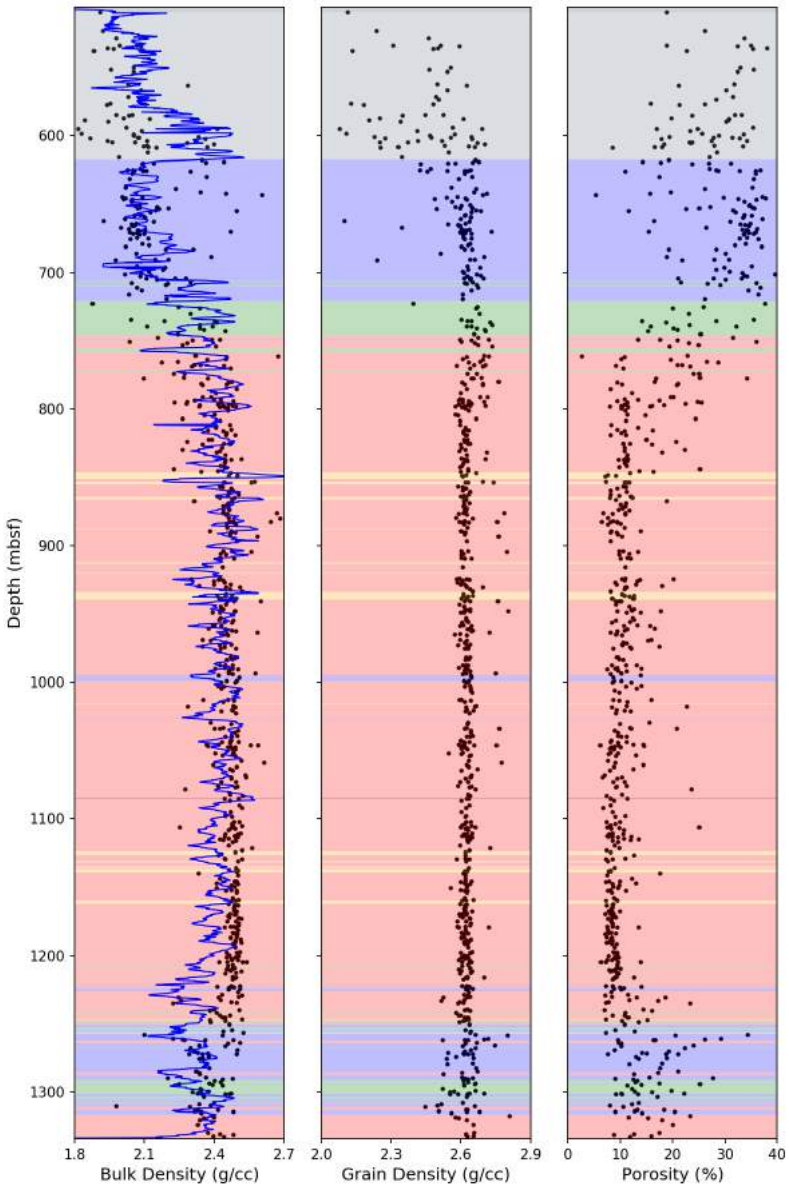

Figure S3. IODP-ICDP Expedition 364 density and porosity data, black dots indicate measurements on discrete samples, the blue line indicates MSCL measurements. Background colours indicate the stratigraphy of Hole M0077A (see Figure S1). Data from *Morgan et al.* (2017).

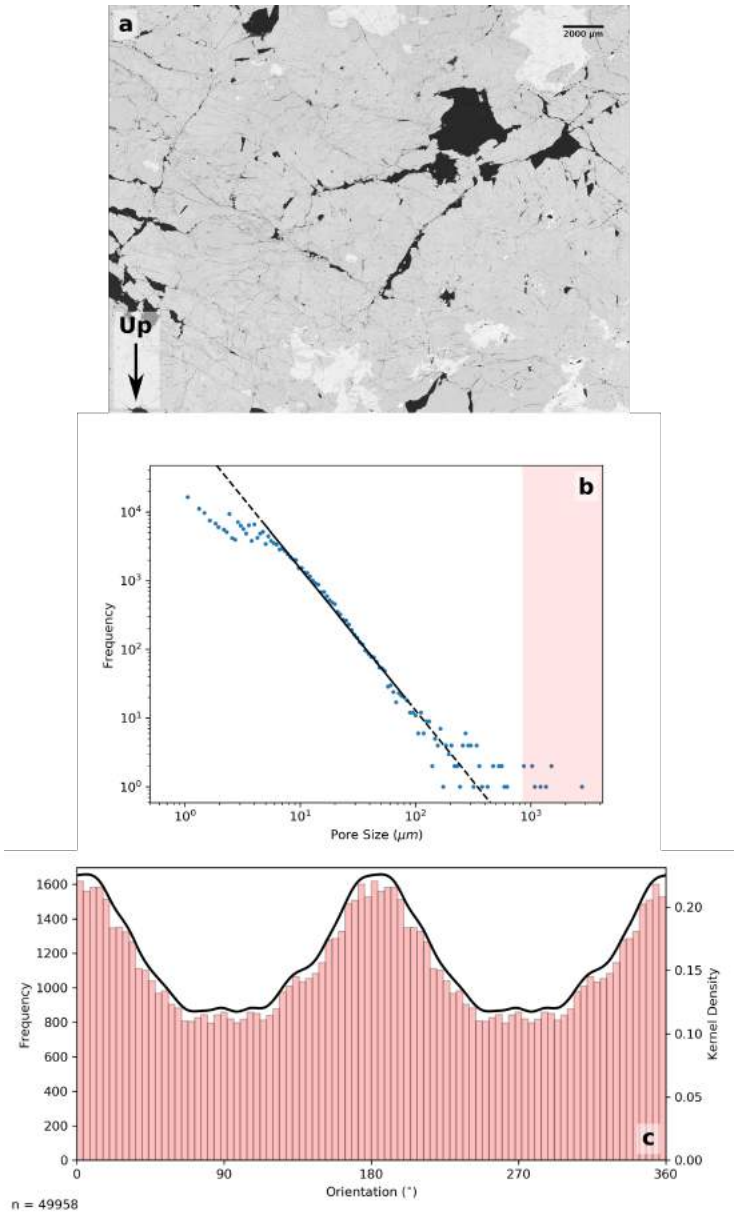

Figure S4. Sample 364-77-A-095-R-3-27-29 (745.16 mbsf). a) Stitched BSE SEM image of the sample. The up-direction of the core is indicated. b) Pore size-frequency distribution of the sample, the area highlighted in pink shows the sizes of pores considered to be anomalously large (where the fitted power-law distribution, black line, has an expected frequency < 0.1), and classified as "inter-granular pores". c) Pore orientation histogram and probability density estimate. Orientation is measured counter-clockwise as a bearing relative to the page orientation, data was adjusted to account for thin section orientation on Figure 6.

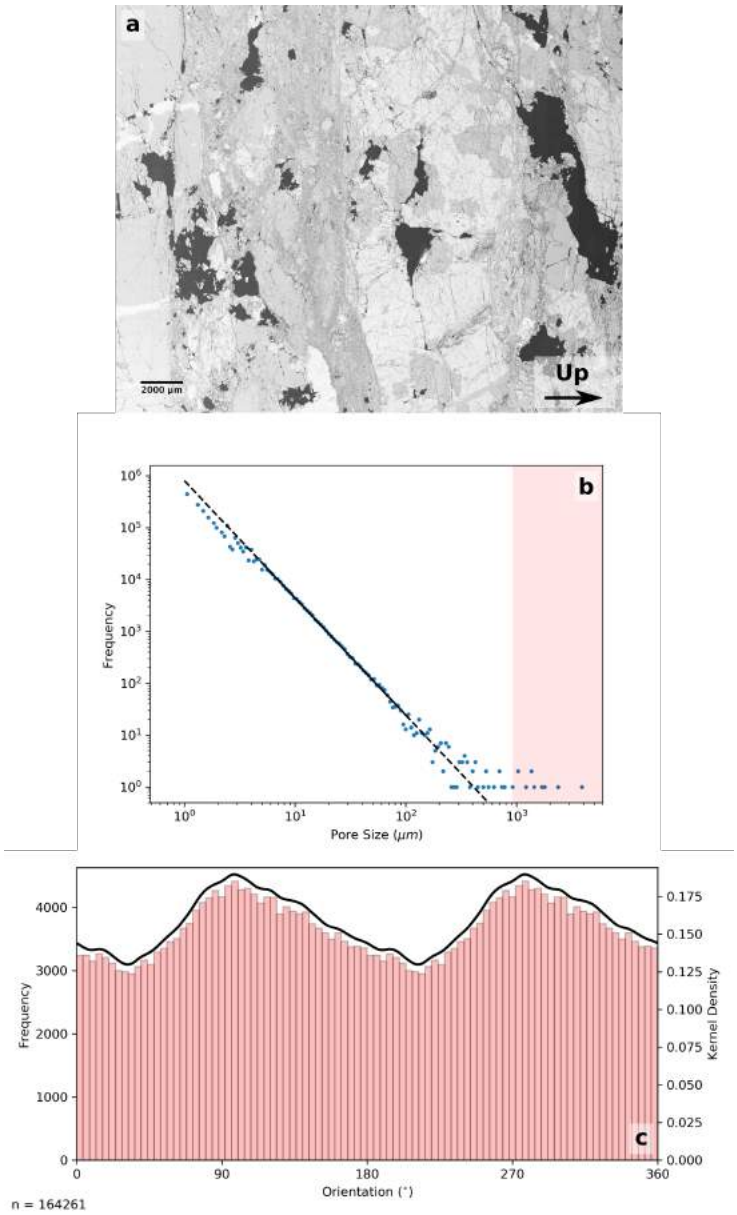

Figure S5. Sample 364-77-A-104-R-1-24-26 (768.59 mbsf). a) Stitched BSE SEM image of the sample. The up-direction of the core is indicated. b) Pore size-frequency distribution of the sample, the area highlighted in pink shows the sizes of pores considered to be anomalously large (where the fitted power-law distribution, black line, has an expected frequency < 0.1), and classified as "inter-granular pores". c) Pore orientation histogram and probability density estimate. Orientation is measured counter-clockwise as a bearing relative to the page orientation, data was adjusted to account for thin section orientation on Figure 6.

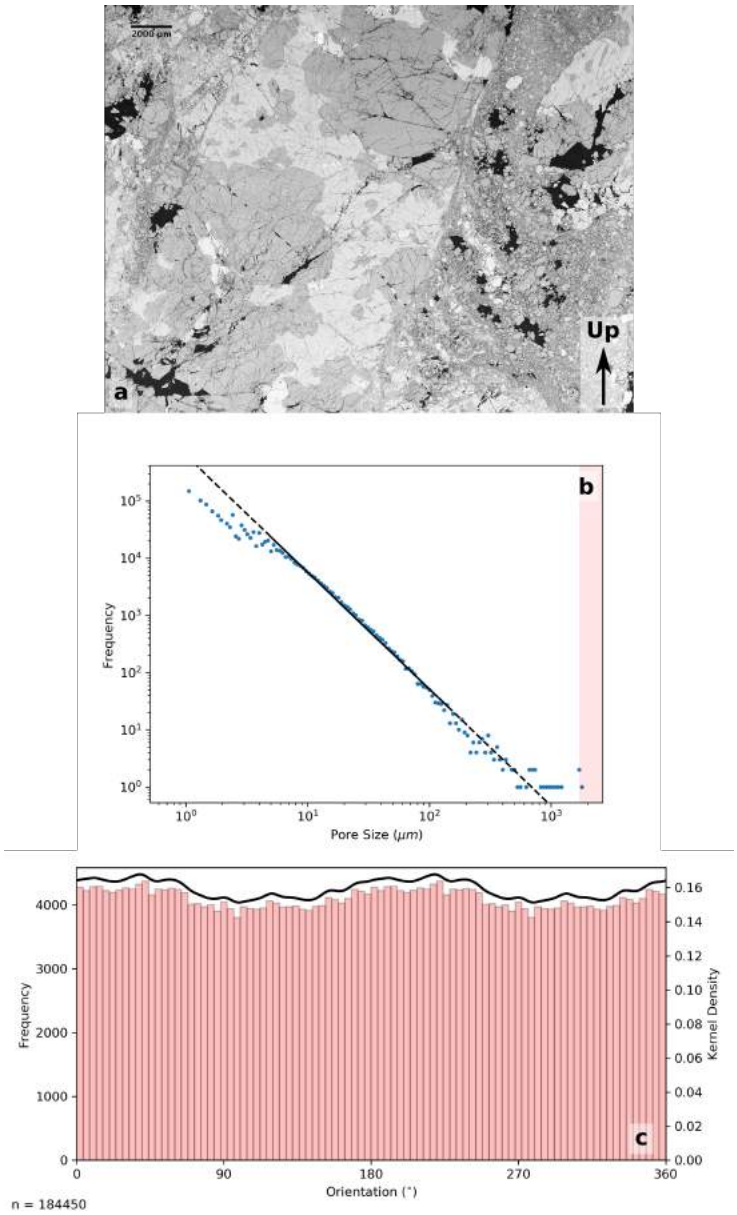

Figure S6. Sample 364-77-A-121-R-1-75-77 (814.85 mbsf). a) Stitched BSE SEM image of the sample. The up-direction of the core is indicated. b) Pore size-frequency distribution of the sample, the area highlighted in pink shows the sizes of pores considered to be anomalously large (where the fitted power-law distribution, black line, has an expected frequency < 0.1), and classified as "inter-granular pores". c) Pore orientation histogram and probability density estimate. Orientation is measured counter-clockwise as a bearing relative to the page orientation, data was adjusted to account for thin section orientation on Figure 6.

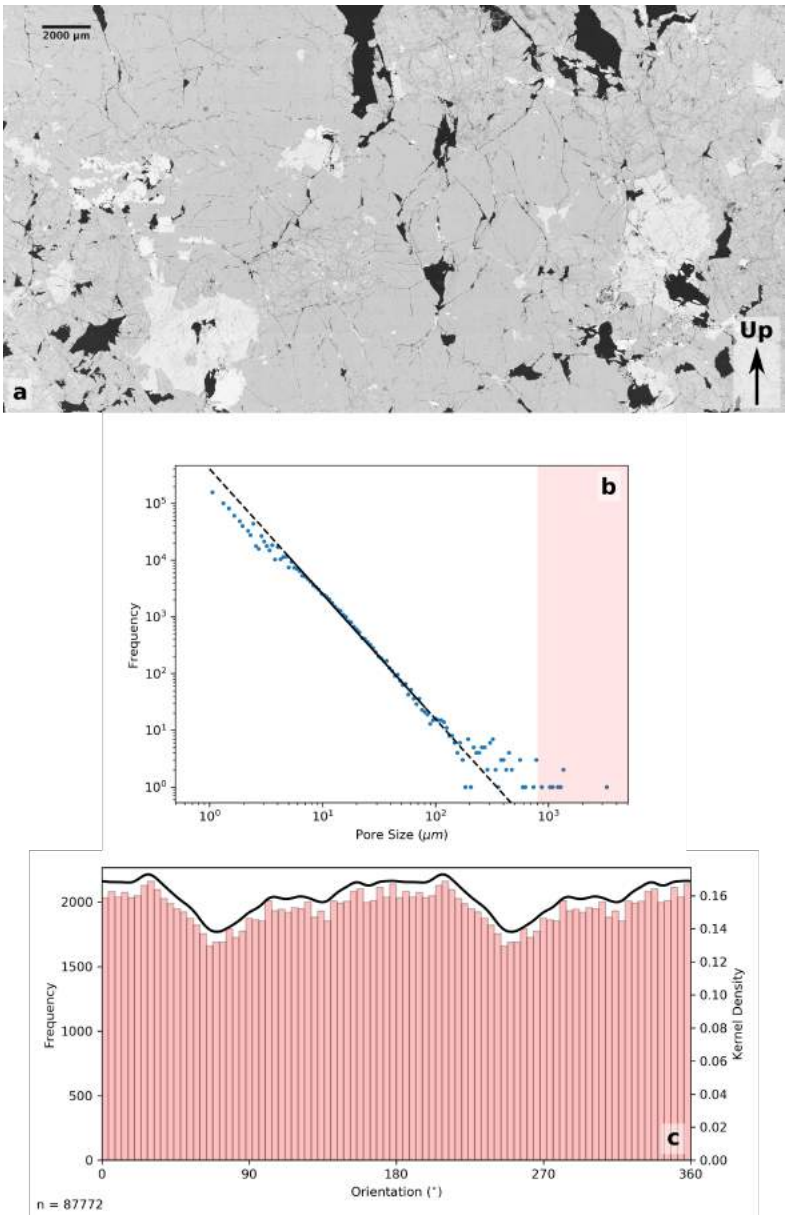

Figure S7. Sample 364-77-A-132-R-1-22-24 (838.45 mbsf). a) Stitched BSE SEM image of the sample. The up-direction of the core is indicated. b) Pore size-frequency distribution of the sample, the area highlighted in pink shows the sizes of pores considered to be anomalously large (where the fitted power-law distribution, black line, has an expected frequency < 0.1), and classified as "inter-granular pores". c) Pore orientation histogram and probability density estimate. Orientation is measured counter-clockwise as a bearing relative to the page orientation, data was adjusted to account for thin section orientation on Figure 6.

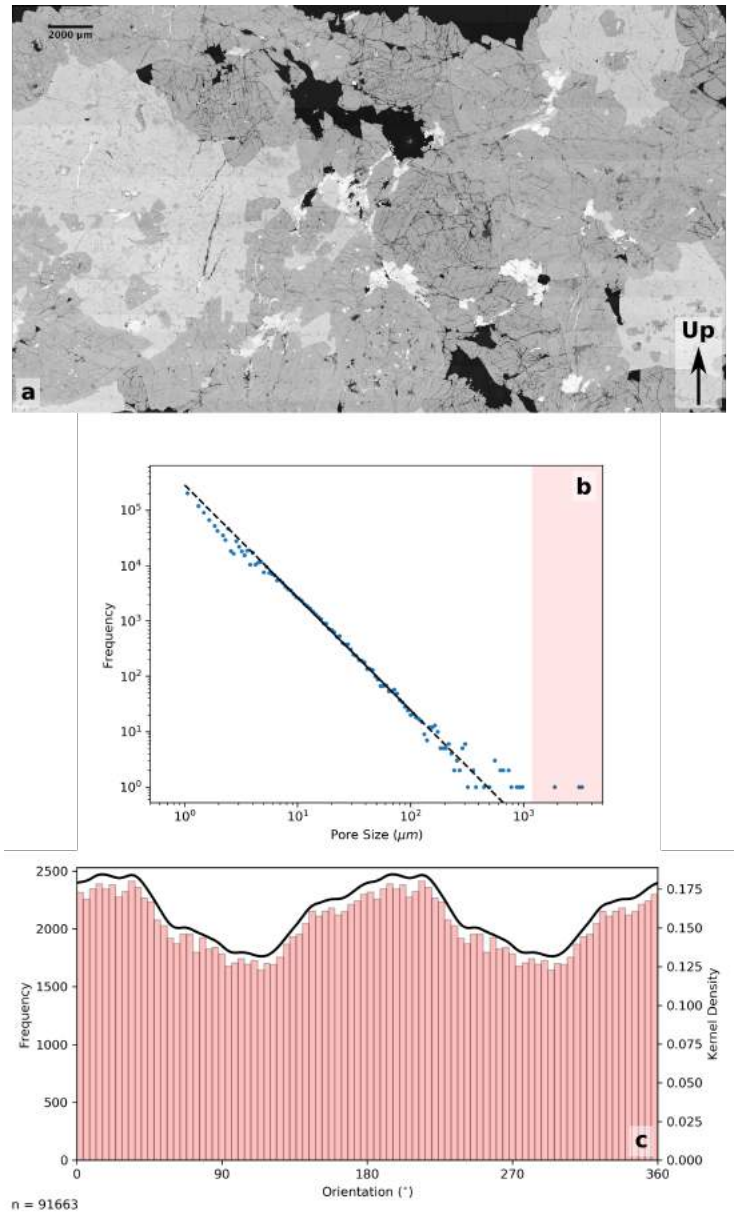

Figure S8. Sample 364-77-A-150-R-1-53-55 (884.43 mbsf). a) Stitched BSE SEM image of the sample. The up-direction of the core is indicated. b) Pore size-frequency distribution of the sample, the area highlighted in pink shows the sizes of pores considered to be anomalously large (where the fitted power-law distribution, black line, has an expected frequency < 0.1), and classified as "inter-granular pores". c) Pore orientation histogram and probability density estimate. Orientation is measured counter-clockwise as a bearing relative to the page orientation, data was adjusted to account for thin section orientation on Figure 6.

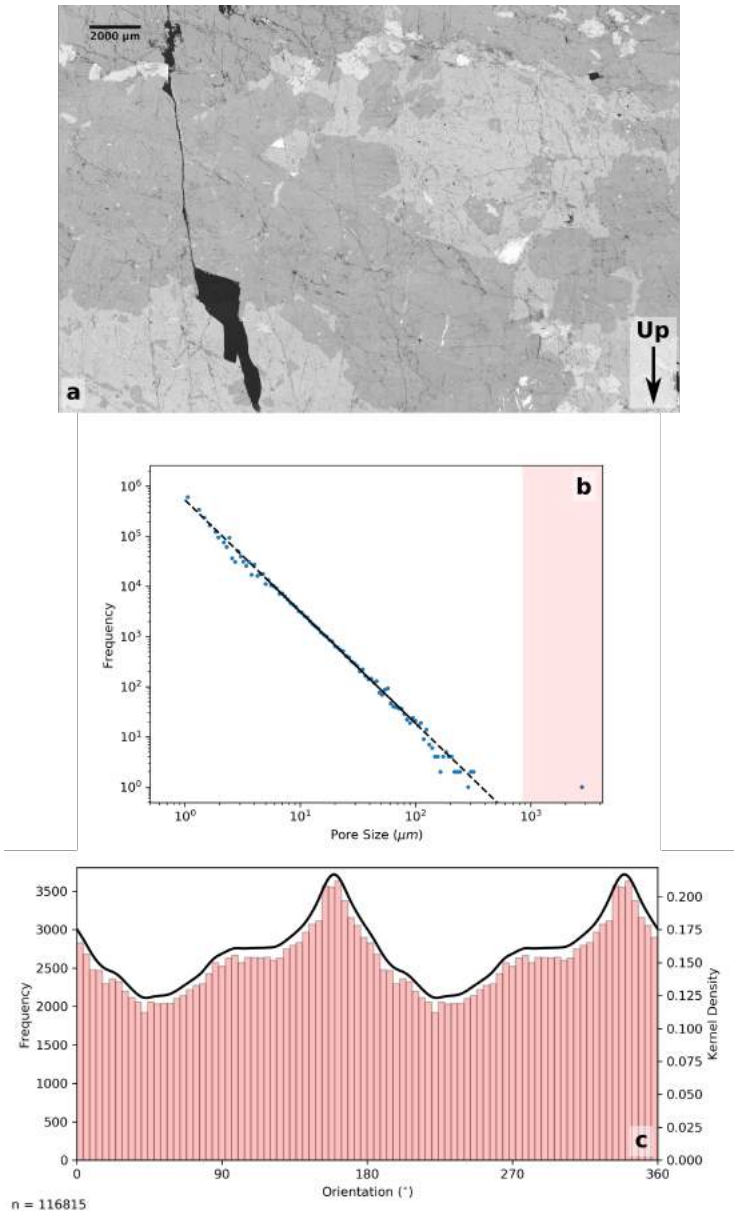

Figure S9. Sample 364-77-A-204-R-1-07-09 (1030.00 mbsf). a) Stitched BSE SEM image of the sample. The up-direction of the core is indicated. b) Pore size-frequency distribution of the sample, the area highlighted in pink shows the sizes of pores considered to be anomalously large (where the fitted power-law distribution, black line, has an expected frequency < 0.1), and classified as "inter-granular pores". c) Pore orientation histogram and probability density estimate. Orientation is measured counter-clockwise as a bearing relative to the page orientation, data was adjusted to account for thin section orientation on Figure 6.

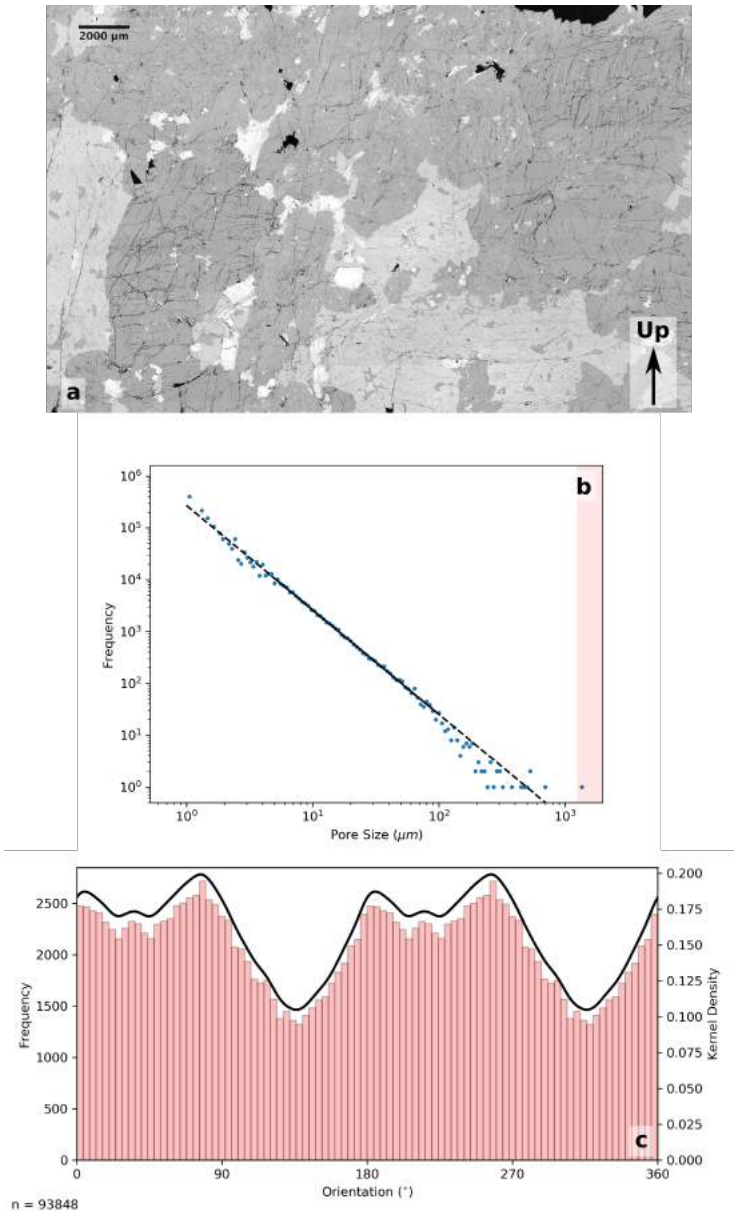

Figure S10. Sample 364-77-A-219-R-1-22-24 (1076.15 mbsf). a) Stitched BSE SEM image of the sample. The up-direction of the core is indicated. b) Pore size-frequency distribution of the sample, the area highlighted in pink shows the sizes of pores considered to be anomalously large (where the fitted power-law distribution, black line, has an expected frequency < 0.1), and classified as "inter-granular pores". c) Pore orientation histogram and probability density estimate. Orientation is measured counter-clockwise as a bearing relative to the page orientation, data was adjusted to account for thin section orientation on Figure 6.

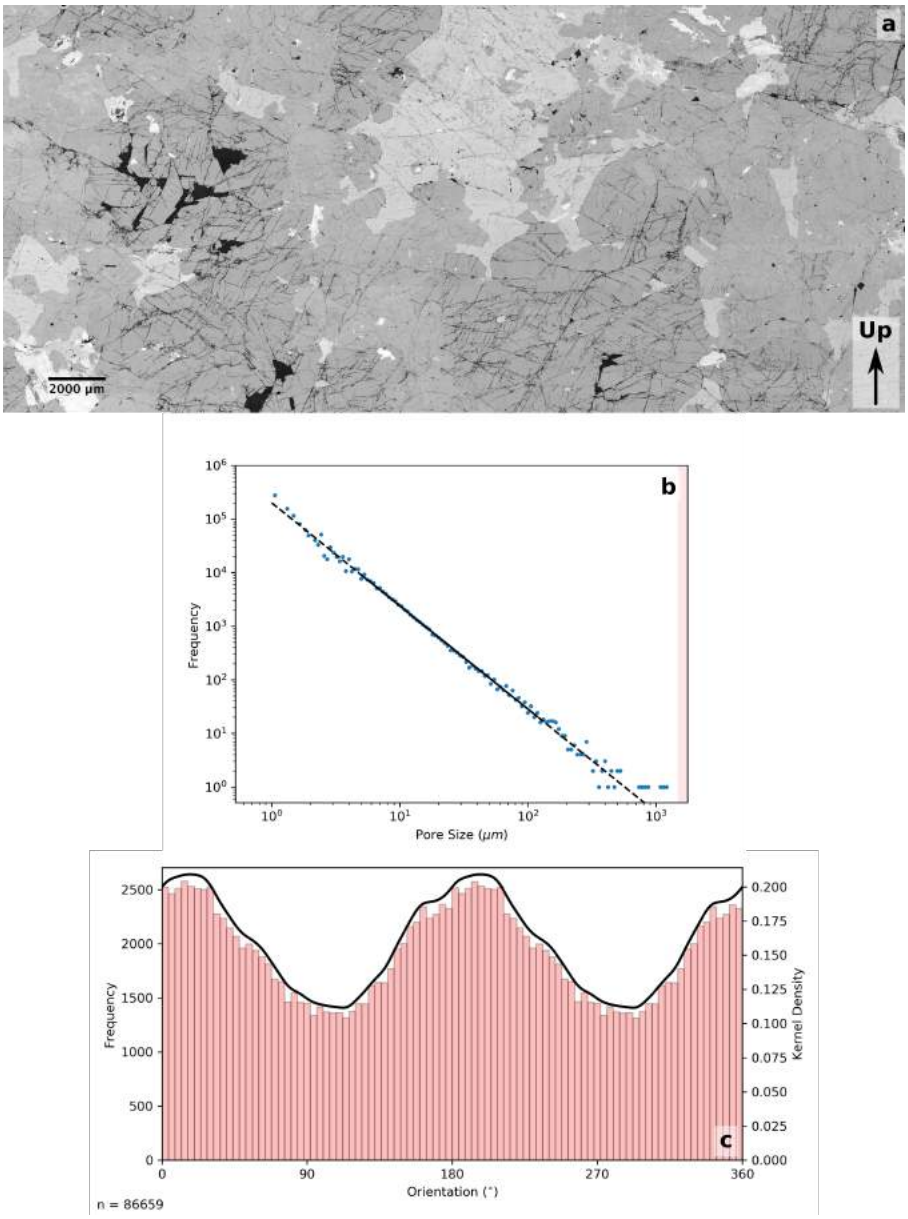

Figure S11. Sample 364-77-A-250-R-1-41-43 (1169.71 mbsf). a) Stitched BSE SEM image of the sample. The up-direction of the core is indicated. b) Pore size-frequency distribution of the sample, the area highlighted in pink shows the sizes of pores considered to be anomalously large (where the fitted power-law distribution, black line, has an expected frequency < 0.1), and classified as "inter-granular pores". c) Pore orientation histogram and probability density estimate. Orientation is measured counter-clockwise as a bearing relative to the page orientation, data was adjusted to account for thin section orientation on Figure 6.

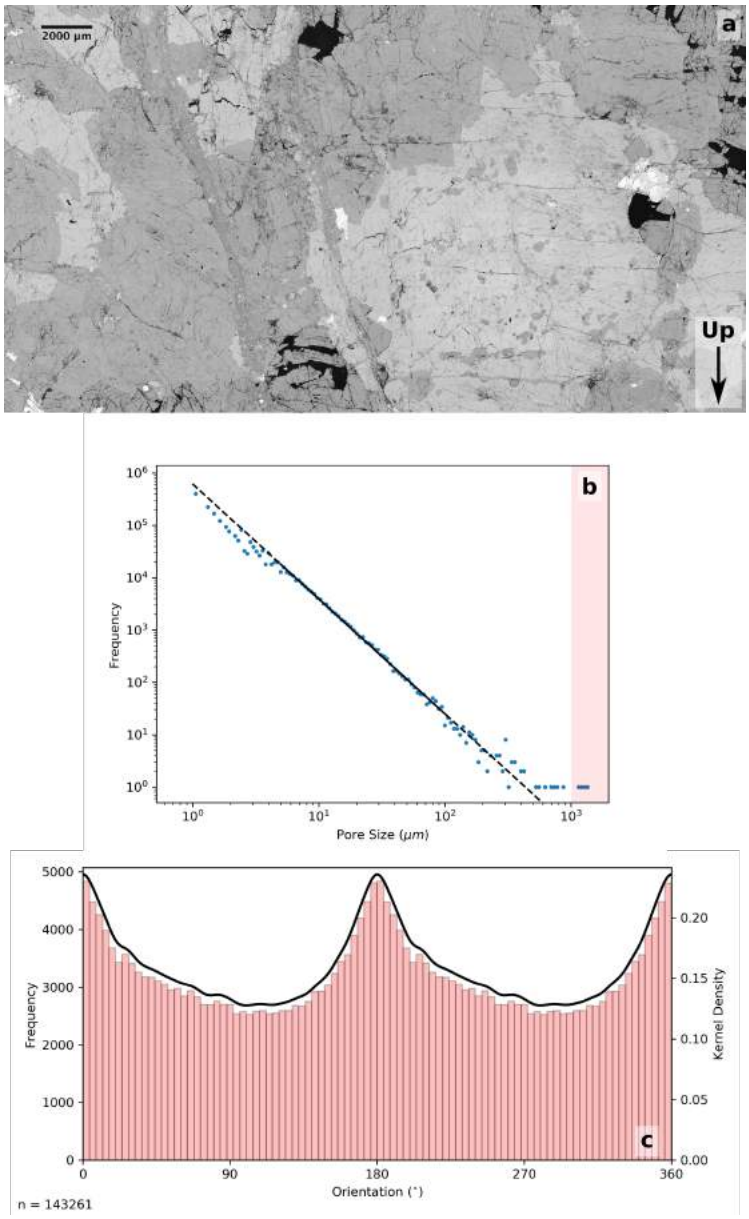

Figure S12. Sample 364-77-A-276-R-1-17-19 (1249.52 mbsf). a) Stitched BSE SEM image of the sample. The up-direction of the core is indicated. b) Pore size-frequency distribution of the sample, the area highlighted in pink shows the sizes of pores considered to be anomalously large (where the fitted power-law distribution, black line, has an expected frequency < 0.1), and classified as "inter-granular pores". c) Pore orientation histogram and probability density estimate. Orientation is measured counter-clockwise as a bearing relative to the page orientation, data was adjusted to account for thin section orientation on Figure 6.

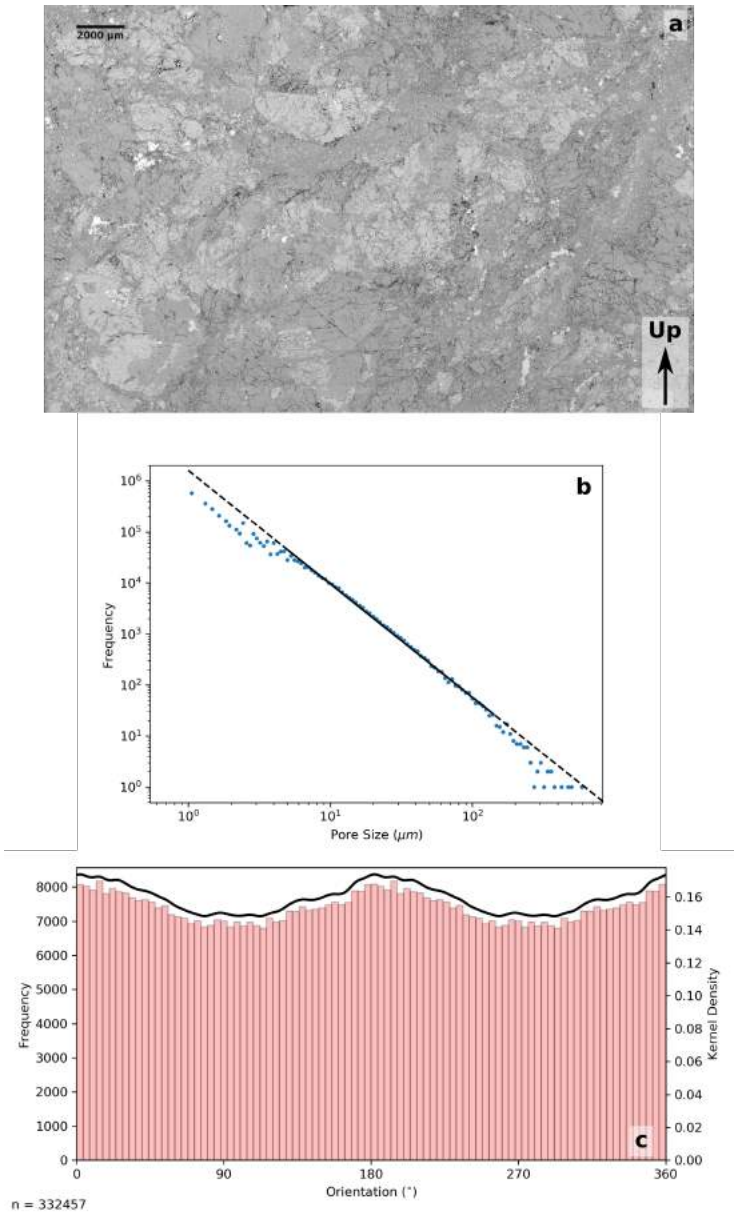

Figure S13. Sample 364-77-A-301-R-1-30-32 (1326.89 mbsf). a) Stitched BSE SEM image of the sample. The up-direction of the core is indicated. b) Pore size-frequency distribution of the sample, the area highlighted in pink shows the sizes of pores considered to be anomalously large (where the fitted power-law distribution, black line, has an expected frequency < 0.1), and classified as "inter-granular pores". c) Pore orientation histogram and probability density estimate. Orientation is measured counter-clockwise as a bearing relative to the page orientation, data was adjusted to account for thin section orientation on Figure 6.

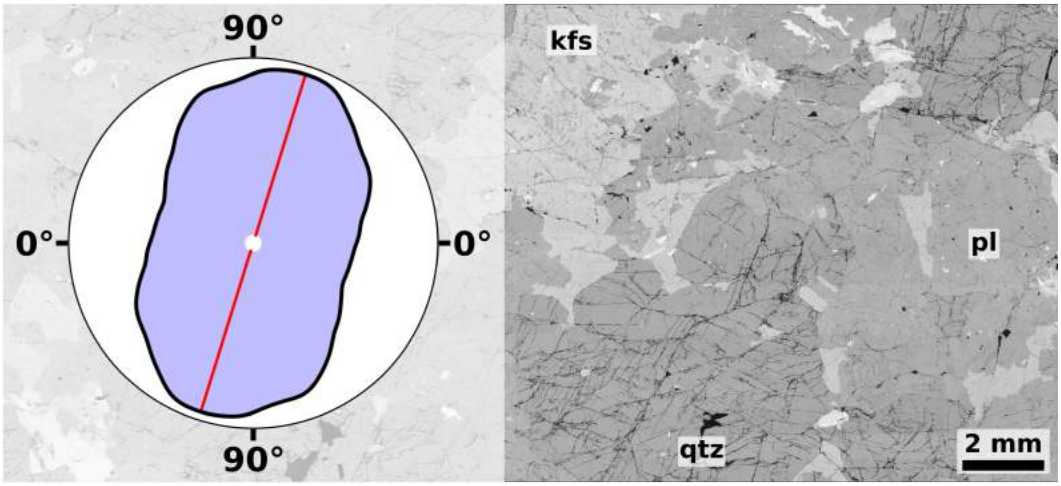

Figure S14. BSE image of Sample 364-77-A-250-R-1-41-43 with its pore orientation-frequency distribution. qtz = Quartz, kfs = Alkali Feldspar, pl = Plagioclase. The dominant orientation (72.7° apparent dip) of pores within the distribution is caused by a dominant set of PFs in multiple quartz grains. Additionally, quartz makes the largest contribution to the total porosity of the sample.

2 Simulating the Chicxulub Impact Event

In this section of Supplementary Material, the parameters of the iSALE model used in the main body of this contribution are shown (Tables S2 and S3). These parameters are exactly the same as used by *Rae et al.* (2019). Post-processing of the results of the iSALE simulation were used in this contribution to determine the predicted orientation of micro-fractures. iSALE input files and the post-processing script to calculate the orientation of principal stresses can be found in the **Additional Supplementary Material** of *Rae et al.* (2019), located at `https://github.com/ImperialCollegeLondon/Chicxulub_StressStrain`. In addition, Figure S15 shows a sequence of selected timesteps from the simulation, highlighting the location of peak-ring material.

Table S2. Global model parameters, more specifically: details of the Eulerian grid, impactor parameters, and details of the initial conductive-convective temperature profile.

Parameter	Symbol	Units	Value
Cell resolution		m	100
Cells per impactor radius			60
Horizontal cells in high resolution zone			1000
Horizontal cells in outer extension zone			200
Vertical cells in high resolution zone			800
Vertical cells in upper extension zone			0
Vertical cells in lower extension zone			200
Impactor velocity	v_i	km s^{-1}	15
Impactor density	ρ_i	kg m^{-3}	2670
Acceleration due to gravity	g	m s^{-2}	9.81
Surface temperature	T_{surf}	K	288
Surface temperature gradient	T_{grad}	K m^{-1}	0.01
Lithospheric thickness	d_{lith}	km	100

Table S3. Material model parameters, more specifically: strength model parameters, damage model parameters, thermal softening parameters, acoustic fluidisation parameters, and dilatancy parameters.

Parameter	Symbol	Units	Mantle (Dunite)	Crust (Granite)	Sediments (Calcite)
Reference Density	ρ	kg m^{-3}	3320	2670	2600
Poisson's ratio	ν		0.25	0.30	0.30
Intact cohesive strength	Y_0	MPa	10	10	5
Intact friction coefficient	μ_i		1.2	2.0	1.0
Intact and damaged strength limit	Y_m	MPa	3500	2500	500
Damaged cohesive strength	Y_{d0}	MPa	0.01	0.01	0.01
Damaged friction coefficient	μ_{di}		0.6	0.6	0.4
Minimum failure strain for low pressure states	ε_{fb}		1×10^{-4}	1×10^{-4}	1×10^{-4}
Constant of proportionality between failure strain and pressure	B		1×10^{-11}	1×10^{-11}	1×10^{-11}
Pressure above which failure is compressional	P_c	MPa	300	300	300
Melt Temperature	T_m	K	1373	1673	1500
Thermal softening coefficient	ξ		1.2	1.2	1.2
Constant in Simon Approximation	p_{bp}		6×10^9	6×10^9	6×10^9
Exponent in Simon Approximation	y_{t0}		3.00	4.05	3.00
Acoustically Fluidized effective kinematic viscosity	η	m^2 s^{-1}	7.5×10^5	7.5×10^5	7.5×10^5
Acoustic Fluidization decay time	T_dec	s	180	180	180
Vibrational particle velocity as a fraction of particle velocity	C_{vib}		0.1	0.1	0.1
Maximum vibrational particle velocity	Vib_{max}	m s^{-1}	200	200	200
Time after which no new acoustic vibrations are generated	t_{off}	s	16	16	16
Maximum dilatancy coefficient	β_{max}		0.09	0.09	0.09
Dilatancy pressure limit	p_{lim}	MPa	200	200	200
Critical distension	α_c		1.2	1.2	1.2
Critical friction coefficient	μ_c		0.4	0.4	0.4
Initial distension	α_0		1.0	1.0	1.0
Minimum distension	α_{min}		1.0	1.0	1.0

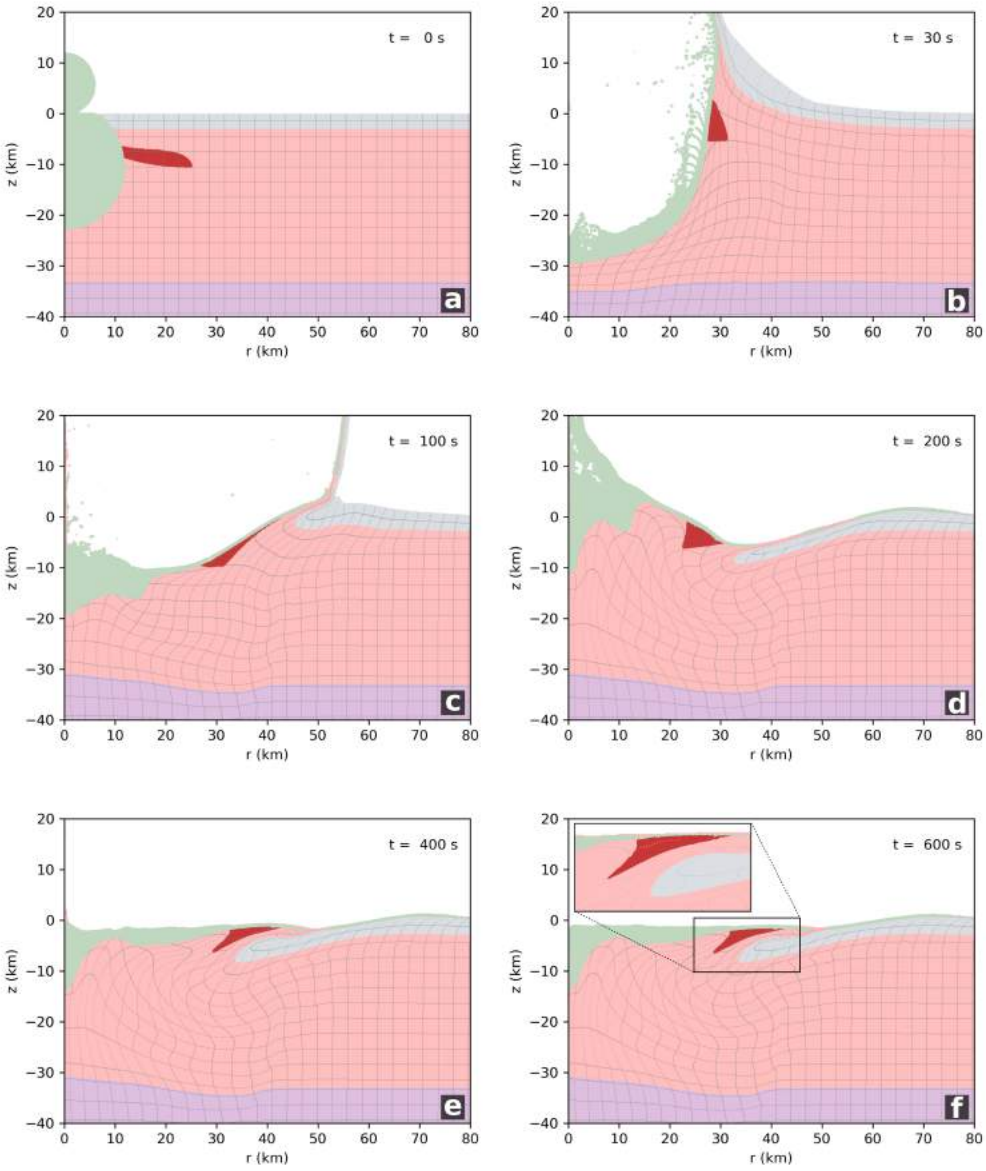

Figure S15. Selected timesteps of the formation of the Chicxulub peak ring. The target is comprised of three layers; sedimentary rock (grey), granitic basement (pink), and mantle (purple). A grid of tracer particles is shown to highlight the sub-crater deformation. Additionally, in the first frame, a), the provenance of impact melt is shown in green and the peak ring material is shown in red. The impact melt and peak ring material is then tracked throughout the steps b) – f) *Rae et al.* (2019)

3 Comparative Data

Here, we present a reproduction of a table from *Pilkington and Grieve* (1992), listing impact structures and the comparative density between fractured and undisturbed target rocks, including the results from this study (Table S4).

Table S4. Density contrasts between fractured and undisturbed target rocks at several terrestrial impact structures. Adapted from *Pilkington and Grieve* (1992).

	Target Rocks	$\nabla\rho$ (kg m^{-3})	Apparent Diameter (km)	Reference
Brent, Canada	Crystalline	170–340*	3.8	*Millman et al.* (1960)
Gosses Bluff, Australia	Sedimentary	150	22	*Barlow* (1979)
Holleford, Canada	Crystalline	240*	2.35	*Beals* (1960)
Manicouagan, Canada	Crystalline	130	85	*Sweeney* (1978)
Nicholson Lake, Canada	Crystalline	70–140	12.5	*Dence et al.* (1968)
Söderfjärden, Finland	Crystalline	160	6.6	*Lauren et al.* (1978)
West Clearwater Lake, Canada	Crystalline	170	36	*Plante et al.* (1990)
Chicxulub, Mexico	Crystalline	184**	200	This study

*Values include effects of sediments and breccias.

**Assuming initial granitic target rocks had no initial porosity, i.e., that the grain density of the granitic rocks is the same as the initial, pre-impact, bulk density of the granitic rocks

References

Barlow, B. (1979), Gravity investigations of the Gosses Bluff impact structure, central Australia, *Bur. Min. Res. J. Aust. Geol. Geophys*, *4*, 323–339, type: dataset.

Beals, C. (1960), A probable meteorite of Precambrian age at Holleford, Ontario, *Publications of the Dominion Observatory, Ottawa.*, *24*, 117–42.

Dence, M., M. Innes, and P. Robertson (1968), Recent geological and geophysical studies of Canadian craters., *Contributions from the Dominion Astrophysical Observatory in Victoria*, *8*.

Gulick, S., G. Christeson, P. Barton, R. Grieve, J. Morgan, and J. Urrutia-Fucugauchi (2013), Geophysical Characterization of the Chicxulub Impact Crater, *Reviews of Geophysics*, *51*(1), 31–52, doi:10.1002/rog.20007.

Lauren, L., J. Lehtovaara, R. Bostrom, and R. Tynni (1978), On the geology of the circular depression at Soderfjarden, western Finland, *Bulletin of the Geological Survey of Finland*, *297*, 1–38.

Millman, P., B. Liberty, J. Clark, P. Willmore, and M. Innes (1960), The Brent Crater, *Publications of the Dominion Observatory, Ottawa.*, *24*, 1–43.

Morgan, J., S. Gulick, T. Bralower, E. Chenot, G. Christeson, P. Claeys, C. Cockell, G. S. Collins, M. J. L. Coolen, L. Ferrire, C. Gebhardt, K. Goto, H. Jones, D. A. Kring, E. L. Ber, J. Lofi, X. Long, C. Lowery, C. Mellett, R. Ocampo-Torres, G. R. Osinski, L. Perez-Cruz, A. Pickersgill, M. Poelchau, A. Rae, C. Rasmussen, M. Rebolledo-Vieyra, U. Riller, H. Sato, D. R. Schmitt, J. Smit, S. Tikoo, N. Tomioka, J. Urrutia-Fucugauchi, M. Whalen, A. Wittmann, K. E. Yamaguchi, and W. Zylberman (2016), The formation of peak rings in large impact craters, *Science*, *354*(6314), 878–882, doi:10.1126/science.aah6561.

Morgan, J., S. Gulick, C. Mellet, S. Green, and Expedition 364 Scientists (2017), *Chicxulub: Drilling the K-Pg Impact Crater*, *Proceedings of the International Ocean Discovery Program*, vol. 364, International Ocean Discovery Program, doi:10.14379/iodp.proc.364.2017.

Pilkington, M., and R. Grieve (1992), The geophysical signature of terrestrial impact craters, *Reviews of Geophysics*, *30*(2), 161–181, doi:10.1029/92RG00192.

Plante, L., M. Seguin, and J. Rondot (1990), tude gravimtrique des astroblmes du Lac l'Eau Claire, Nouveau-Qubec, *Geoexploration*, *26*(4), 303–323, doi:10.1016/0016-7142(90)90010-P.

Rae, A., G. Collins, M. Poelchau, U. Riller, T. Davison, R. Grieve, G. Osinski, J. Morgan, and IODP-ICDP Expedition 364 Scientists (2019), Stress-Strain Evolution during Peak-Ring Formation: A Case Study of the Chicxulub Impact Structure, *Journal of Geophysical Research: Planets*, *124*(2), 396–417.

Sweeney, J. F. (1978), Gravity study of great impact, *Journal of Geophysical Research: Solid Earth*, *83*(B6), 2809–2815.